PHYSICAL REVIEW C **90**, 034904 (2014)

Azimuthal anisotropy of D-meson production in Pb-Pb collisions at $\sqrt{s_{NN}} = 2.76$ TeV

B. Abelev *et al.**

(ALICE Collaboration)

(Received 9 May 2014; published 10 September 2014)

The production of the prompt charmed mesons D^0, D^+, and D^{*+} relative to the reaction plane was measured in Pb-Pb collisions at a center-of-mass energy per nucleon-nucleon collision of $\sqrt{s_{\rm NN}} = 2.76$ TeV with the ALICE detector at the CERN Large Hadron Collider. D mesons were reconstructed via their hadronic decays at central rapidity in the transverse-momentum ($p_{\rm T}$) interval 2–16 GeV/c. The azimuthal anisotropy is quantified in terms of the second coefficient v_2 in a Fourier expansion of the D-meson azimuthal distribution and in terms of the nuclear modification factor $R_{\rm AA}$, measured in the direction of the reaction plane and orthogonal to it. The v_2 coefficient was measured with three different methods and in three centrality classes in the interval 0%–50%. A positive v_2 is observed in midcentral collisions (30%–50% centrality class), with a mean value of $0.204^{+0.099}_{-0.036}$ (tot. unc.) in the interval $2 < p_{\rm T} < 6$ GeV/c, which decreases towards more central collisions (10%–30% and 0%–10% classes). The positive v_2 is also reflected in the nuclear modification factor, which shows a stronger suppression in the direction orthogonal to the reaction plane for midcentral collisions. The measurements are compared to theoretical calculations of charm-quark transport and energy loss in high-density strongly interacting matter at high temperature. The models that include substantial elastic interactions with an expanding medium provide a good description of the observed anisotropy. However, they are challenged to simultaneously describe the strong suppression of high-$p_{\rm T}$ yield of D mesons in central collisions and their azimuthal anisotropy in noncentral collisions.

DOI: 10.1103/PhysRevC.90.034904 PACS number(s): 25.75.Dw, 24.10.Nz, 25.75.Ag

I. INTRODUCTION

Collisions of heavy nuclei at ultrarelativistic energies are expected to lead to the formation of a high-density color-deconfined state of strongly interacting matter. According to calculations of quantum chromodynamics (QCD) on the lattice (see, e.g., [1–4]), a phase transition to the quark-gluon plasma (QGP) state can occur in these collisions, when conditions of high-energy density and temperature are reached. Heavy quarks (charm and beauty), with large masses $m_{\rm c} \approx 1.3$ and $m_{\rm b} \approx 4.5$ GeV/c^2, are produced in pairs predominantly at the initial stage of the collision [5] in hard scattering processes characterized by time scales shorter than the medium formation time. They traverse the medium and interact with its constituents via both inelastic (medium-induced gluon radiation, i.e., radiative energy loss) [6,7] and elastic (collisional) [8] QCD processes. Heavy-flavor hadrons are thus effective probes of the properties of the medium formed in the collisions.

Compelling evidence for heavy-quark energy loss in strongly interacting matter is provided by the observation of a modification of the transverse-momentum ($p_{\rm T}$) distributions of heavy-flavor hadrons. This modification is quantified by the nuclear modification factor $R_{\rm AA}(p_{\rm T}) = dN_{\rm AA}/dp_{\rm T} \big/ \langle T_{\rm AA}\rangle\, d\sigma_{\rm pp}/dp_{\rm T}$, where $dN_{\rm AA}/dp_{\rm T}$ is the differential yield in nucleus-nucleus collisions in a given centrality class, $d\sigma_{\rm pp}/dp_{\rm T}$ is the cross section in pp collisions, and $\langle T_{\rm AA}\rangle$ is the average nuclear overlap function [9]. In central nucleus-nucleus collisions at BNL Relativistic Heavy Ion Collider (RHIC) and CERN Large Hadron Collider (LHC) energies, $R_{\rm AA}$ values significantly below unity were observed for heavy-flavor hadrons with $p_{\rm T}$ values larger than a few GeV/c [10–15]. A suppression by a factor up to 3–5 ($R_{\rm AA} \approx 0.25$) at $p_{\rm T} \simeq 5$ GeV/c was measured in central collisions for inclusive electrons and muons from heavy-flavor hadron decays, both at RHIC ($\sqrt{s_{\rm NN}} = 200$ GeV), by the PHENIX and STAR Collaborations [10,11], and at the LHC ($\sqrt{s_{\rm NN}} = 2.76$ TeV), by the ALICE Collaboration [14]. At the LHC, the effect was also measured separately for charm, via D mesons by the ALICE Collaboration [13], and for beauty, via nonprompt J/ψ particles from B hadron decays by the CMS Collaboration [15].

The D-meson suppression at RHIC and at the LHC is described (see Refs. [12,13]) by model calculations that implement a combination of mechanisms of heavy-quark interactions with the medium, via radiative and collisional processes, as well as in-medium formation and dissociation of charmed hadrons [16–22]. Model comparisons with more differential measurements can provide important insights into the relevance of the various interaction mechanisms and the properties of the medium. In particular, the dependence of the partonic energy loss on the in-medium path length is expected to be different for each mechanism (linear for collisional processes [8] and close to quadratic for radiative processes [7]). In addition, it is an open question whether low-momentum heavy quarks participate, through interactions with the medium, in the collective expansion of the system and whether they can reach thermal equilibrium with the medium constituents [23,24]. It was also suggested that low-momentum heavy quarks could hadronize not only via fragmentation in the vacuum, but also via the mechanism of recombination with other quarks from the medium [24,25].

*Full author list given at the end of the article.

These questions can be addressed with azimuthal anisotropy measurements of heavy-flavor hadron production with respect to the reaction plane, defined by the beam axis and the impact parameter of the collision. For noncentral collisions, the two nuclei overlap in an approximately lenticular region, the short axis of which lies in the reaction plane. Hard partons are produced at an early stage, when the geometrical anisotropy is not yet reduced by the system expansion. Therefore, partons emitted in the direction of the reaction plane (in plane) have, on average, a shorter in-medium path length than partons emitted orthogonally (out of plane), leading *a priori* to a stronger high-p_{T} suppression in the latter case. In the low-momentum region, the in-medium interactions can also modify the parton emission directions, thus translating the initial spatial anisotropy into a momentum anisotropy of the final-state particles. Both effects cause a momentum anisotropy that can be characterized with the coefficients v_n and the symmetry planes Ψ_n of the Fourier expansion of the p_{T}-dependent particle distribution $d^2N/dp_{\mathrm{T}}d\varphi$ in azimuthal angle φ. The elliptic flow is the second Fourier coefficient v_2, which can also be expressed as the average over all particles in all events of the angular correlation $\cos[2(\varphi - \Psi_2)]$. The symmetry planes Ψ_n for all harmonics would coincide with the reaction plane if nuclei were spherically symmetric with a matter density depending only on the distance from the center of the nucleus. Owing to fluctuations in the positions of the participant nucleons, the plane of symmetry fluctuates event by event around the reaction plane, independently for each harmonic, so that the Ψ_n directions no longer coincide.

A path-length-dependent energy loss, which gives a positive v_2, is considered to be the dominant contribution to the azimuthal anisotropy of charged hadrons in the high-p_{T} region, above 8–10 GeV/c [26,27]. At low p_{T}, a large v_2 is considered as evidence for the collective hydrodynamical expansion of the medium [28,29]. Measurements of light-flavor hadron v_2 over a large p_{T} range at RHIC and LHC are generally consistent with these expectations [18,30–36]. In contrast to light quarks and gluons, which can be produced or annihilated during the entire evolution of the medium, heavy quarks are produced predominantly in initial hard scattering processes and their annihilation rate is small [5]. Thus, the final-state heavy-flavor hadrons at all transverse momenta originate from heavy quarks that experienced each stage of the system evolution. High-momentum heavy quarks quenched by in-medium energy loss are shifted towards low momenta and, while participating in the collective expansion, they may ultimately thermalize in the system. In this context, the measurement of D meson v_2 is also important for the interpretation of recent results on J/ψ anisotropy [37], because J/ψ mesons formed from $c\bar{c}$ recombination would inherit the azimuthal anisotropy of their constituent quarks [38,39].

An azimuthal anisotropy in heavy-flavor production was observed in Au-Au collisions at RHIC with v_2 values of up to about 0.13 for electrons from heavy-flavor decays [10]. The measured asymmetry is reproduced by several models [19–21,40–45] implementing heavy-quark transport within a medium that undergoes a hydrodynamical expansion. The transport properties, i.e., the diffusion coefficients, of heavy quarks in the medium can be related to its shear viscosity [40]. For LHC energies these models predict a large v_2 (in the range 0.10–0.20 in semicentral collisions) for D mesons at $p_{\mathrm{T}} \approx 2$–3 GeV/c and a decrease to a constant value $v_2 \approx 0.05$ at high p_{T}. The models described in Refs. [20,42–45] include, at the hadronization stage, a contribution from the recombination of charm quarks with light quarks from the medium, which enhances v_2 at low p_{T}.

The measurement of the D meson v_2 in the centrality class 30%–50% in Pb-Pb collisions at $\sqrt{s_{\mathrm{NN}}} = 2.76$ TeV, carried out using the ALICE detector, was presented in Ref. [46]. The v_2 coefficient was found to be significantly larger than zero in the interval $2 < p_{\mathrm{T}} < 6$ GeV/c and comparable in magnitude with that of charged particles.

Here the measurement is extended to other centrality classes and accompanied with a study of the azimuthal dependence of the nuclear modification factor with respect to the reaction plane. The decays $D^0 \to K^-\pi^+$, $D^+ \to K^-\pi^+\pi^+$ and $D^{*+} \to D^0\pi^+$ and charge conjugates were reconstructed. The v_2 coefficient was measured with various methods in the centrality class 30%–50% as a function of p_{T}. For the D^0 meson, which has the largest statistical significance, the centrality dependence of v_2 in the range 0%–50% is presented and the anisotropy is also quantified in terms of the nuclear modification factor R_{AA} in two 90°-wide azimuthal intervals centered around the in-plane and out-of-plane directions.

The experimental apparatus is presented in Sec. II. The data analysis is described in Sec. III, including the data sample, the D-meson reconstruction, and the anisotropy measurement methods. Systematic uncertainties are discussed in Sec. IV. The results on v_2 and R_{AA} are presented in Sec. V and compared with model calculations in Sec. VI.

II. EXPERIMENTAL APPARATUS

The ALICE apparatus is described in Ref. [47]. In this section, the characteristics of the detectors used for the D-meson analyses are summarized. The z axis of the ALICE coordinate system is defined by the beam direction, the x axis lies in the horizontal plane and is pointing towards the center of the LHC accelerator ring, and the y axis is pointing upward.

Charged-particle tracks are reconstructed in the central pseudorapidity[1] region ($|\eta| < 0.9$) with the time projection chamber (TPC) and the inner tracking system (ITS). For this analysis, charged hadron identification was performed using information from the TPC and the time-of-flight (TOF) detectors. These detectors are located inside a large solenoidal magnet that provides a field with a strength of 0.5 T, parallel to the beam direction. Two VZERO scintillator detectors, located in the forward and backward pseudorapidity regions, are used for online event triggering, collision centrality determination and, along with the zero-degree calorimeter (ZDC), for offline event selection.

The ITS [48] includes six cylindrical layers of silicon detectors surrounding the beam vacuum tube, at radial distances

[1]The pseudorapidity is defined as $\eta = -\ln(\tan\vartheta/2)$, where ϑ is the polar angle with respect to the z axis.

from the nominal beam line ranging from 3.9 cm for the innermost layer to 43 cm for the outermost one. The two innermost layers consist of silicon pixel detectors (SPDs) with a pixel size of $50 \times 425\ \mu\text{m}^2$ ($r\varphi \times z$, in cylindrical coordinates), providing an intrinsic spatial resolution of 12 μm in $r\varphi$ and 100 μm in z. The third and fourth layers use silicon drift detectors (SDDs) with an intrinsic spatial resolution of 35 and 25 μm in $r\varphi$ and z, respectively. The two outermost layers of the ITS contain double-sided silicon strip detectors (SSDs) with an intrinsic spatial resolution of 20 μm in $r\varphi$ and 830 μm in the z direction. The alignment of the ITS sensor modules is crucial for the precise space point reconstruction needed for the heavy-flavor analyses. It was performed using survey information, cosmic-ray tracks, and pp data. A detailed description of the employed methods can be found in Ref. [48]. The effective spatial resolution along the most precise direction, $r\varphi$, is about 14, 40, and 25 μm, for SPD, SDD, and SSD, respectively [48,49].

The TPC [50] covers the pseudorapidity interval $|\eta| < 0.9$ and extends in radius from 85 to 247 cm. Charged-particle tracks are reconstructed and identified with up to 159 space points. The transverse-momentum resolution for tracks reconstructed with the TPC and the ITS ranges from about 1% at $p_{\text{T}} = 1$ GeV/c to about 2% at 10 GeV/c, both in pp and Pb-Pb collisions. The TPC also provides a measurement of the specific energy deposition dE/dx, with up to 159 samples. The truncated mean method, using only the lowest 60% of the measured dE/dx samples, gives a Gaussian distribution with a resolution (ratio of σ over centroid) of about 6%, which is slightly dependent on the track quality and on the detector occupancy.

The TOF detector [51] is positioned at a radius of 370–399 cm and it has the same pseudorapidity coverage as the TPC ($|\eta| < 0.9$). The TOF provides an arrival time measurement for charged tracks with an overall resolution, including the measurement of the event start time, of about 80 ps for pions and kaons at $p_{\text{T}} = 1$ GeV/c in the Pb-Pb collision centrality range used in this analysis [51].

The VZERO detector [52] consists of two arrays of scintillator counters covering the pseudorapidity regions $-3.7 < \eta < -1.7$ (VZERO-C) and $2.8 < \eta < 5.1$ (VZERO-A). Each array is composed of 8×4 segments in the azimuthal and radial directions, respectively. This detector provides a low-bias interaction trigger (see Sec. III A). For Pb-Pb collisions, the signal amplitude from its segments is used to classify events according to centrality, while the azimuthal segmentation allows for an estimation of the reaction plane.

The ZDCs are located on either side of the interaction point at $z \approx \pm 114$ m. The timing information from the neutron ZDCs was used to reject parasitic collisions between one of the two beams and residual nuclei present in the vacuum tube.

III. DATA ANALYSIS

A. Data sample and event selection

The analysis was performed on a data sample of Pb-Pb collisions recorded in November and December 2011 at a center-of-mass energy per nucleon-nucleon collision of $\sqrt{s_{\text{NN}}} = 2.76$ TeV. The events were collected with an interaction trigger based on information from the VZERO detector, which required coincident signals recorded in the detectors at forward and backward pseudorapidities. An online selection based on the VZERO signal amplitude was used to enhance the sample of central and midcentral collisions through two separate trigger classes. Events were further selected offline to remove background coming from parasitic beam interactions by using the time information provided by the VZERO and the neutron ZDC detectors. Only events with a reconstructed interaction point (primary vertex), determined by extrapolating charged-particle tracks, within ± 10 cm from the center of the detector along the beam line were used in the analysis.

TABLE I. Number of events and integrated luminosity for the considered centrality classes, expressed as percentiles of the hadronic cross section. The uncertainty on the integrated luminosity derives from the uncertainty of the hadronic Pb-Pb cross section from the Glauber model [9,53].

Centrality class (%)	N_{events}	$L_{\text{int}}(\mu\text{b}^{-1})$
0–10	16.0×10^6	20.9 ± 0.7
10–30	9.5×10^6	6.2 ± 0.2
30–50	9.5×10^6	6.2 ± 0.2

Collisions were classified in centrality classes, determined from the sum of the amplitudes of the signals in the VZERO detector and defined in terms of percentiles of the total hadronic Pb-Pb cross section. To relate the centrality classes to the collision geometry, the distribution of the VZERO summed amplitudes was fitted by a model based on the Glauber approach for the geometrical description of the nuclear collision [9] complemented by a two-component model for particle production [53]. The centrality classes used in the analysis are reported in Table I, together with the number of events in each class and the corresponding integrated luminosity.

B. D-meson reconstruction

The D^0, D^+, and D^{*+} mesons and their antiparticles were reconstructed in the rapidity interval $|y| < 0.8$ via their hadronic decay channels $D^0 \to K^-\pi^+$ (with branching ratio, BR, of $3.88 \pm 0.05\%$), $D^+ \to K^-\pi^+\pi^+$ (BR = $9.13 \pm 0.19\%$), and $D^{*+} \to D^0\pi^+$ (BR = $67.7 \pm 0.5\%$) and their corresponding charge conjugates [54]. The D^0 and D^+ mesons decay weakly with mean proper decay lengths ($c\tau$) of approximately 123 and 312 μm [54]. The D^{*+} meson decays strongly at the primary vertex.

D^0 and D^+ candidates were defined from pairs and triplets of tracks within the fiducial acceptance $|\eta| < 0.8$, selected by requiring at least 70 associated space points in the TPC, $\chi^2/\text{ndf} < 2$ for the momentum fit, and at least two associated hits in the ITS, with at least one of them in the SPD. A transverse-momentum threshold $p_{\text{T}} > 0.4$ GeV/c was applied to reduce the combinatorial background. D^{*+} candidates were obtained by combining the D^0 candidates with tracks selected with the same requirements as described above, but with a

lower transverse-momentum threshold $p_{\rm T} > 0.1$ GeV/c and at least three associated hits in the ITS, with at least one of them in the SPD. The lower $p_{\rm T}$ threshold was used because the momentum of the pions from D^{*+} decays is typically low, as a consequence of the small mass difference between D^{*+} and D^0.

The selection of tracks with $|\eta| < 0.8$ introduces a steep drop in the acceptance of D mesons for rapidities larger than 0.7–0.8, depending on $p_{\rm T}$. A fiducial acceptance region was, therefore, defined as $|y| < y_{\rm fid}(p_{\rm T})$, with $y_{\rm fid}(p_{\rm T})$ increasing from 0.7 to 0.8 in $2 < p_{\rm T} < 5$ GeV/c and taking a constant value of 0.8 for $p_{\rm T} > 5$ GeV/c [13]. The D-meson v_2 results are not expected to be affected by this small variation in rapidity acceptance.

The D-meson yields were measured with an invariant mass analysis of reconstructed decays, using kinematic and geometrical selection criteria, and particle identification (PID). The selection of D^0 and D^+ decays was based on the reconstruction of secondary vertices with a separation of a few hundred microns from primary vertex. In the case of the D^{*+} decay, the secondary vertex of the produced D^0 was reconstructed. The coordinates of the primary vertex and of the secondary vertices, as well as the corresponding covariance matrices, were computed using a χ^2 minimization method [55].

The selection strategy is the same as in previous pp [55,56] and Pb-Pb [13] analyses. It exploits the displacement of the decay tracks from the primary vertex (transverse impact parameter, d_0), the separation between the secondary and primary vertices (decay length, L) and the pointing of the reconstructed meson momentum to the primary vertex.

The transverse impact parameter d_0 of a given track is defined as the signed distance of closest approach of the extrapolated track to the primary vertex in the (x, y) plane. The sign of d_0 is attributed based on the position of the primary vertex with respect to the curve of the (x, y) projection of the track. In Pb-Pb collisions, the impact parameter resolution in the transverse direction is better than 65 μm for tracks with a transverse momentum larger than 1 GeV/c and reaches 20 μm for $p_{\rm T} > 20$ GeV/c [13]. This includes the contribution from the primary vertex precision, which is better than 10 μm in the central and semicentral Pb-Pb events used in this analysis. The impact parameter measurement is significantly less precise along the longitudinal direction, e.g., 170 μm at $p_{\rm T} = 1$ GeV/c.

A pointing condition was applied via a selection on the angle $\vartheta_{\rm pointing}$ between the direction of the reconstructed momentum of the candidate and the straight line connecting the primary and secondary vertices. For Pb-Pb collisions, two additional selection variables were introduced with respect to pp analyses, namely the projection of the pointing angle and of the decay length onto the transverse plane ($\vartheta^{xy}_{\rm pointing}$ and L^{xy}). The selection requirements were tuned so as to provide a large statistical significance for the signal and to keep the selection efficiency as high as possible. The chosen selection values depend on the $p_{\rm T}$ of the D meson and become more stringent from peripheral to central collisions.

The selection criteria for the centrality class 30%–50% are described in the following. The D^0 candidates were selected by requiring the decay tracks to have an impact parameter significance $|d_0|/\sigma_{d_0} > 0.5$ (σ_{d_0} is the uncertainty on the track impact parameter) and to form a secondary vertex with a track-to-track distance of closest approach smaller than 250–300 μm, depending on $p_{\rm T}$, and a decay length larger than 100 μm. The product of the decay track impact parameters, which are of opposite sign for well-displaced signal topologies, was required to be below $-(200\ \mu{\rm m})^2$ for low-$p_{\rm T}$ candidates (2–3 GeV/c) and below $-(120\ \mu{\rm m})^2$ for high-$p_{\rm T}$ candidates (12–16 GeV/c), with a smooth variation between these values in 2–12 GeV/c. A significance of the projection of the decay length in the transverse plane $L^{xy}/\sigma_{L^{xy}}$ (where $\sigma_{L^{xy}}$ is the uncertainty on L^{xy}) larger than 5 was also required. A selection on the angle ϑ^* between the kaon momentum in the D^0 rest frame and the boost direction was used to reduce the contamination from background candidates that do not represent real two-body decays and typically have large values of $|\cos\vartheta^*|$. The selection $|\cos\vartheta^*| < 0.8$ was applied. The pointing of the D^0 momentum to the primary vertex was implemented by requiring $\cos\vartheta_{\rm pointing} > 0.95$ and $\cos\vartheta^{xy}_{\rm pointing} > 0.998$ at low $p_{\rm T}$ (2–3 GeV/c). Because the background is lower at high $p_{\rm T}$, the cuts were progressively made less stringent for increasing $p_{\rm T}$. In the 0%–10% and 10%–30% centrality classes the combinatorial background is larger than in 30%–50%. Therefore, the selections were made more stringent and they are similar to those used for the 0%–20% centrality class in Ref. [13].

The D^+ candidates were selected by requiring a decay length larger than 1200–1600 μm, depending on $p_{\rm T}$, and $\cos\vartheta_{\rm pointing}$ larger than 0.998 (0.990) in the $p_{\rm T}$ interval 3–4 (8–12) GeV/c, with a smooth variation in between. Further requirements to reduce the combinatorial background were $\cos\vartheta^{xy}_{\rm pointing} > 0.993$–$0.998$ and $L^{xy}/\sigma_{L^{xy}} > 9$–$11$, depending on the candidate $p_{\rm T}$. In general, the D^+ selection criteria are more stringent than those of the D^0 because of the larger combinatorial background.

In the D^{*+} analysis, the selection of the decay D^0 candidates was similar to that used for the D^0 analysis. Only D^0 candidates with invariant mass within 2.5σ of the world-average D^0 mass [54] were used, where σ is the $p_{\rm T}$-dependent Gaussian σ of the invariant mass distribution observed in data. The decay pion was selected with the same track quality criteria as for the D^0 and D^+ decay tracks.

Pions and kaons were identified with the TPC and TOF detectors, on the basis of the difference, expressed in units of the resolution (σ), between the measured signal and that expected for the considered particle species. Compatibility regions at $\pm 3\sigma$ around the expected mean energy deposition dE/dx and TOF were used. Tracks without a TOF signal were identified using only the TPC information. This PID strategy provided a reduction by a factor of about three of the combinatorial background in the low-$p_{\rm T}$ range, while preserving most of the signal (see Sec. III D).

The D^0 and D^+ raw yields were obtained with a fit to the invariant mass M distribution of the D-meson candidates. For the D^{*+} signal the mass difference $\Delta M = M(K^-\pi^+\pi^+) - M(K^-\pi^+)$ was considered. The fit function is the sum of a Gaussian to describe the signal and a term describing the background, which is an exponential for D^0 and D^+ and has

the form $f(\Delta M) = a\,(\Delta M - m_\pi)^b$ for the D^{*+}, where m_π is the charged pion mass and a and b are free parameters. The centroids and the widths of the Gaussian functions were found to be in agreement, respectively, with the D-meson PDG mass values [54] and with the simulation results, confirming that the background fluctuations were not causing a distortion in the signal line shape. An example of invariant mass distributions is shown in Sec. III C.

C. Azimuthal anisotropy analysis methods

The $p_{\rm T}$-differential azimuthal distribution of produced particles can be described by a Fourier series,

$$\frac{d^2N}{d\varphi dp_{\rm T}} = \frac{dN}{2\pi dp_{\rm T}}\left[1 + 2\sum_{n=1}^{\infty} v_n(p_{\rm T})\cos n(\varphi - \Psi_n)\right], \quad (1)$$

where Ψ_n is the initial-state spatial plane of symmetry of the nth harmonic, defined by the geometrical distribution of the nucleons participating in the collision. To determine the second harmonic coefficient v_2, the $\vec{Q}$ vector

$$\vec{Q} = \begin{pmatrix} \sum_{i=1}^{N} w_i \cos 2\varphi_i \\ \sum_{i=1}^{N} w_i \sin 2\varphi_i \end{pmatrix} \quad (2)$$

is defined from the azimuthal distribution of charged particles, where φ_i are the azimuthal angles and N is the multiplicity of charged particles. The weights w_i are discussed later in the text. The charged particles used for the $\vec{Q}$ vector determination are indicated in the following as reference particles (RFPs). The azimuthal angle of the $\vec{Q}$ vector

$$\psi_2 = \frac{1}{2}\tan^{-1}\left(\frac{Q_y}{Q_x}\right) \quad (3)$$

is called event plane angle and it is an estimate of the second harmonic symmetry plane Ψ_2.

The event plane (EP) [57], scalar product (SP) [58], and two-particle cumulant methods [59] were used to measure the D-meson elliptic flow.

The charged-particle tracks used for the $\vec{Q}$ vector determination were selected with the following criteria: at least 50 associated space points in the TPC; $\chi^2/\text{ndf} < 2$ for the momentum fit in the TPC; a distance of closest approach to the primary vertex smaller than 3.2 cm in z and 2.4 cm in the (x,y) plane. To minimize the nonuniformities in the azimuthal acceptance, no requirement was applied on the number of ITS points associated with the track. To avoid autocorrelations between the D-meson candidates and the EP angles, the $\vec{Q}$ vector was calculated for each candidate excluding from the set of RFPs the tracks used to form that particular candidate. Tracks with $p_{\rm T} > 150\ \text{MeV}/c$ were considered and the pseudorapidity interval was limited to the positive region $0 < \eta < 0.8$, where the TPC acceptance and efficiency were more uniform as functions of the azimuthal angle for this data set. The remaining azimuthal nonuniformity was corrected for using weights w_i in Eq. (2), defined as the inverse of the φ distribution of charged particles used for the $\vec{Q}$ vector determination, $1/(dN/d\varphi_i)$, multiplied by a function $f(p_{\rm T}) = \begin{cases} p_{\rm T}/\text{GeV}/c, p_{\rm T} < 2\ \text{GeV}/c \\ 2, p_{\rm T} \geqslant 2\ \text{GeV}/c \end{cases}$. This function mimics the $p_{\rm T}$ dependence of the charged particle v_2 and it improves the estimate of Ψ_2 by enhancing the contribution of particles with a stronger flow signal (see, e.g., Ref. [33]). The distribution of the EP angle ψ_2 obtained for this set of RFPs is shown in Fig. 1(a), for the centrality range 30%–50%. The distribution, divided by its integral, exhibits a residual nonuniformity below 1%.

An additional study was performed with the $\vec{Q}$ vector determined from the azimuthal distribution of signals in the

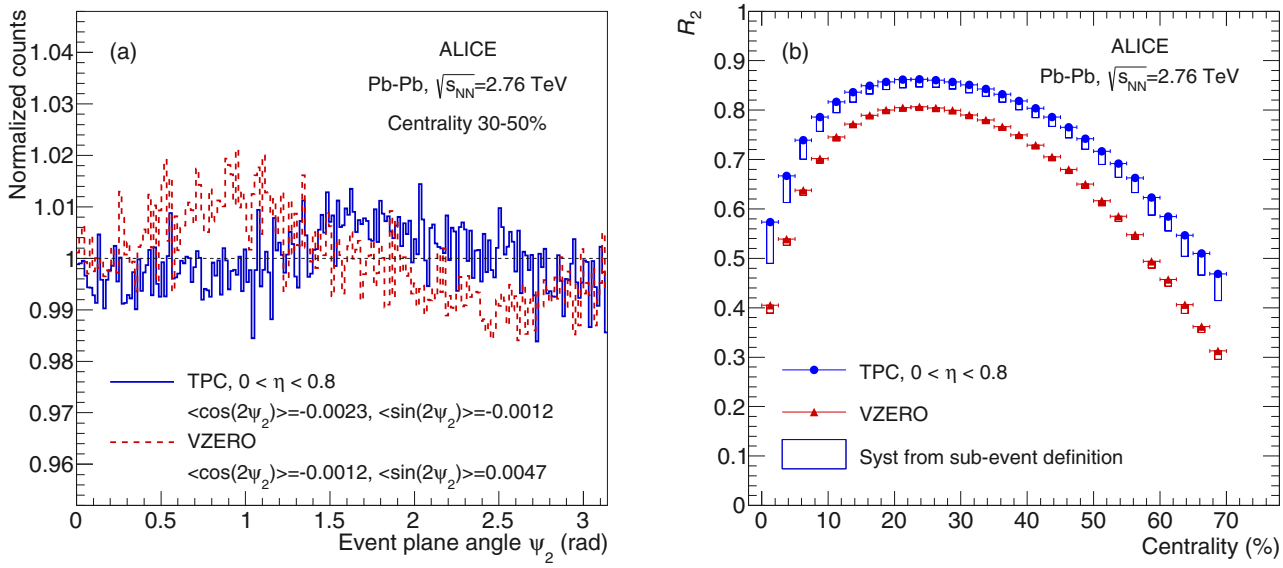

FIG. 1. (Color online) (a) Distribution of EP angle ψ_2, estimated from TPC tracks with $0 < \eta < 0.8$ (solid line) or with the VZERO detector signals (dashed line) in the centrality range 30%–50%. The distributions are normalized by their integral. (b) Event-plane resolution correction factor R_2 as a function of centrality for the TPC and VZERO detectors. The boxes represent the systematic uncertainties estimated from the variation of R_2 when changing the subevents used for its determination.

segments of the VZERO detectors, which are sensitive to particles produced at forward and backward rapidities. The $\vec{Q}$ vector was calculated with Eq. (2), with the sum running over the eight azimuthal sectors of each VZERO detector, where φ_i was defined by the central azimuth of the ith sector, and w_i equal to the signal amplitude in the ith sector for the selected event, which is proportional to the number of charged particles crossing the sector. Nonuniformities in the VZERO acceptance and efficiency were corrected for using the procedure described in Ref. [60]. The residual nonuniformity is about 1%, as shown in Fig. 1(a).

For the EP method, the measured anisotropy $v_2^{\rm obs}$ was divided by the EP resolution correction factor R_2 according to the equation $v_2 = v_2^{\rm obs}/R_2$, with R_2 being smaller than one. This resolution depends on the multiplicity and v_2 of the RFP [57]. For the EP computed using TPC tracks, R_2 was determined from the correlation of the EP angles reconstructed from RFP in the two sides of the TPC, $-0.8 < \eta < 0$ and $0 < \eta < 0.8$, i.e., two samples of tracks (called subevents) with similar multiplicity and v_2. R_2 is shown in Fig. 1(b) as a function of collision centrality. The average R_2 values in the three centrality classes used in this analysis are 0.6953 (0%–10%), 0.8503 (10%–30%), and 0.8059 (30%–50%). The statistical uncertainty on R_2 is negligible ($\sim 10^{-4}$). The systematic uncertainty on R_2 was estimated by using the three-subevent method described in Ref. [61]. In this case, the EPs reconstructed in the TPC ($0 < \eta < 0.8$), VZERO-A ($2.8 < \eta < 5.1$), and VZERO-C ($-3.7 < \eta < -1.7$) were used. This method yielded R_2 values smaller than those obtained from the two-subevents method by 6.9%, 2.0%, and 2.3% for the centrality classes 0%–10%, 10%–30%, and 30%–50%, respectively. A part of this difference can be attributed to the presence of short-range nonflow correlations that are suppressed when the three subevents with a pseudorapidity gap are used. Nonflow correlations can originate from resonance or cascadelike decays and from jets. The resolution of the EP determined from the VZERO detector (summing the signals in VZERO-A and VZERO-C) is also shown in Fig. 1(b). In this case, R_2 was measured with three subevents, namely the signals in the VZERO detector (both A and C sides) and the tracks in the positive and negative η regions of the TPC. The systematic uncertainty was estimated from the difference with the results obtained with two TPC subevents separated by 0.4 units in pseudorapidity (η gap). The EP determination has a poorer resolution with the VZERO detector than with the TPC tracks. As a consequence, the v_2 measurement is expected to be more precise with the TPC EP.

In the EP method, the D-meson yield was measured in two 90°-wide intervals of $\Delta\varphi = \varphi_D - \psi_2$: *in-plane* ($-\frac{\pi}{4} < \Delta\varphi \leqslant \frac{\pi}{4}$ and $\frac{3\pi}{4} < \Delta\varphi \leqslant \frac{5\pi}{4}$) and *out-of-plane* ($\frac{\pi}{4} < \Delta\varphi \leqslant \frac{3\pi}{4}$ and $\frac{5\pi}{4} < \Delta\varphi \leqslant \frac{7\pi}{4}$). φ_D is defined as the azimuthal angle of the D-meson momentum vector at the primary vertex. The invariant mass distributions for the three meson species are shown in Fig. 2 in three $p_{\rm T}$ intervals for the 30%–50% centrality class, along with the fits used for the yield estimation (Sec. III B). When fitting the invariant mass distribution in the two $\Delta\varphi$ intervals, the centroid and the width of the Gaussian functions were fixed, for each meson species and for each $p_{\rm T}$ interval, to those obtained from a fit to the invariant mass distribution integrated over φ, where the statistical significance of the signal is larger.

Integrating Eq. (1) and including the correction for the EP resolution $1/R_2$ yields

$$v_2\{\mathrm{EP}\} = \frac{1}{R_2}\frac{\pi}{4}\frac{N_{\text{in-plane}} - N_{\text{out-of-plane}}}{N_{\text{in-plane}} + N_{\text{out-of-plane}}}. \tag{4}$$

The contribution of higher harmonics to the v_2 value calculated with this equation can be evaluated by integrating the corresponding terms of the Fourier series. All odd harmonics, as well as v_4 and v_8, induce the same average contribution to $N_{\text{in-plane}}$ and $N_{\text{out-of-plane}}$ owing to symmetry, and therefore they do not affect v_2 calculated with Eq. (4). The contribution of v_6, v_{10} and higher harmonics is assumed to be negligible based on the values measured for light-flavor hadrons [34,62].

The measurement of the elliptic flow with the SP method is given by [57]

$$v_2\{\mathrm{SP}\} = \frac{1}{2}\left(\frac{\langle \vec{u}_a \cdot \frac{\vec{Q}_b}{N_b}\rangle}{\sqrt{\langle \frac{\vec{Q}_a}{N_a}\cdot\frac{\vec{Q}_b}{N_b}\rangle}} + \frac{\langle \vec{u}_b \cdot \frac{\vec{Q}_a}{N_a}\rangle}{\sqrt{\langle \frac{\vec{Q}_a}{N_a}\cdot\frac{\vec{Q}_b}{N_b}\rangle}}\right), \tag{5}$$

where $\langle\ \rangle$ indicates an average over D-meson candidates in all events. The vector $\vec{u}$ is defined as $\vec{u} = (\cos 2\varphi_D, \sin 2\varphi_D)$, where φ_D the D-meson candidate momentum azimuthal direction. The $\vec{Q}_{a,b}$ and $\vec{u}_{a,b}$ vectors were computed from charged particles and D-meson candidates, respectively, in two separate pseudorapidity regions: (a) $0 < \eta < 0.8$ and (b) $-0.8 < \eta < 0$. The elliptic flow was computed by correlating D mesons from the positive η region with the charged particles in the negative η region, and vice versa. This separation in pseudorapidity suppresses two-particle correlations at short distance that are attributable to decays ($D^* \to D + X$ and $B \to D^{(*)} + X$). The denominator in Eq. (5) plays a similar role as the resolution correction in the EP method. Because the resolution is proportional to the number of used RFPs, the vectors $\vec{Q}_a$ and $\vec{Q}_b$ were normalized by N_a and N_b, respectively, before averaging over all events. The azimuthal nonuniformity of the TPC response, which results in nonzero average values of $\vec{Q}_a$ and $\vec{Q}_b$, was corrected for using a recentering procedure [57]: $\vec{Q}'_{a,b} = \vec{Q}_{a,b} - \langle \vec{Q}_{a,b}\rangle$.

The two-particle cumulant is defined by the equation [32,59,63]

$$v_2\{2\} = \frac{\langle \vec{u}\cdot\frac{\vec{Q}}{N}\rangle}{\sqrt{\langle \frac{\vec{Q}_a}{N_a}\cdot\frac{\vec{Q}_b}{N_b}\rangle}}. \tag{6}$$

For this method, the azimuthal nonuniformity of the detector acceptance and efficiency was corrected for with the aforementioned recentering procedure. In contrast to the SP method, there is no pseudorapidity gap between the D mesons and the RFP for the two-particle cumulant method.

For both the SP and two-particle cumulant methods, the v_2 of D-meson candidates was computed in narrow intervals of invariant mass M for D^0 and D^+ and mass difference ΔM for the D^{*+}. In each invariant mass interval, the measured v_2 is the weighted average of the D-meson v_2 ($v_2^{\rm S}$) and the background v_2 ($v_2^{\rm B}$) with the weights given by the relative fractions of signal

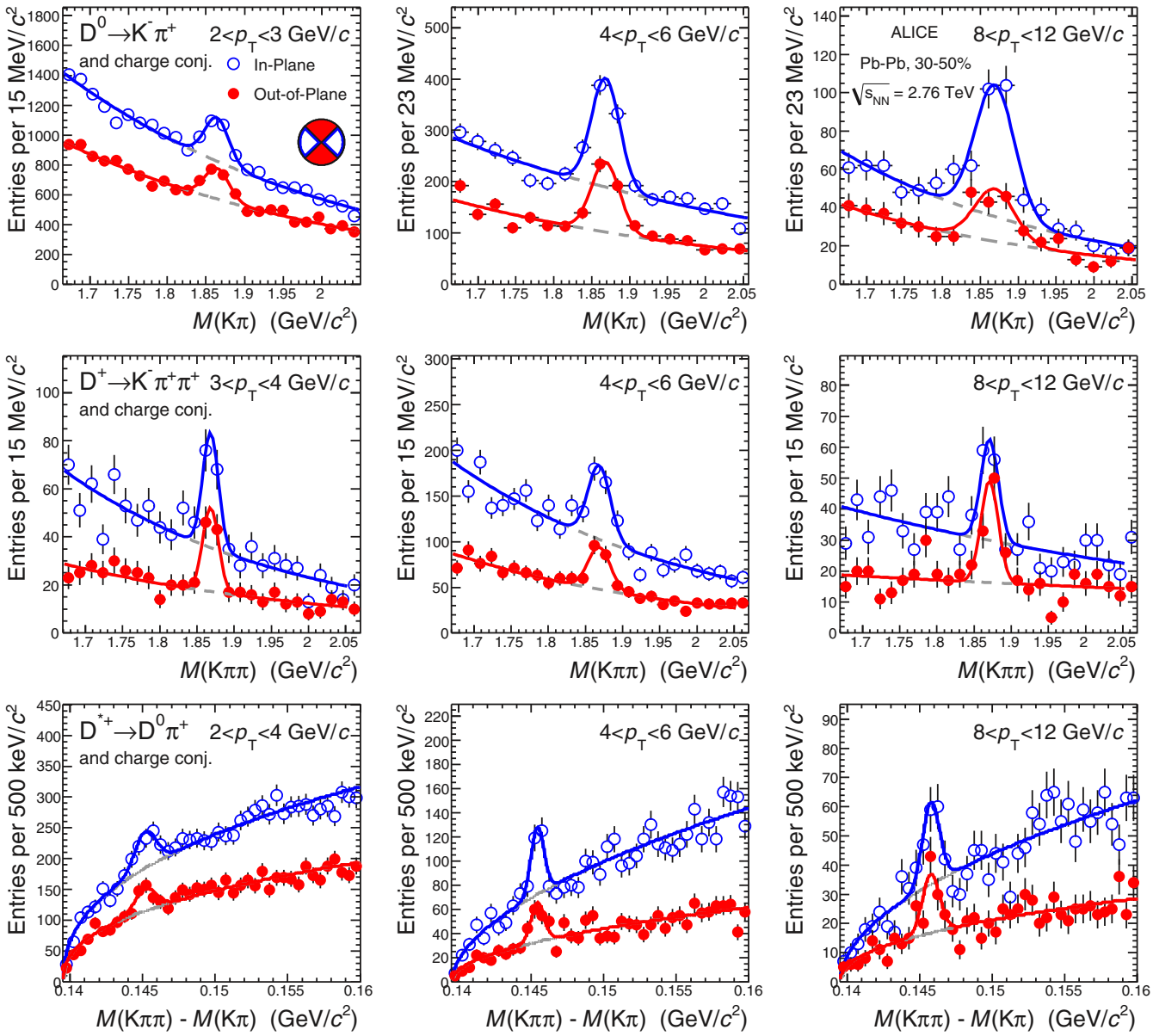

FIG. 2. (Color online) Distributions of the invariant mass for D^0 (top panels) and D^+ (middle panels) candidates and of the mass difference for D^{*+} candidates (bottom panels) in the two $\Delta\varphi$ intervals used in the EP method for Pb-Pb collisions in the 30%–50% centrality class. The rapidity interval is $|y| < y_{\rm fid}$ (see Sec. III B for details). For each meson species three $p_{\rm T}$ intervals are shown, along with the fits used to extract the signal yield. The definition of the two $\Delta\varphi$ intervals is sketched in the top-left panel.

(S) and background (B) in that interval. To extract the values of $v_2^{\rm S}$ and $v_2^{\rm B}$, a simultaneous fit of the distributions of counts and v_2 as a function of invariant mass M was performed. The invariant mass distribution was fitted with a sum of two terms for signal and background, as explained in Sec. III B. The $v_2(M)$ distribution was fitted with a function:

$$v_2(M) = \left[{\rm S}(M)v_2^{\rm S} + {\rm B}(M)v_2^{\rm B}(M)\right]/[{\rm S}(M) + {\rm B}(M)]. \quad (7)$$

The background contribution $v_2^{\rm B}$ was parametrized by a linear function of M. An example of the corresponding distributions and fits is shown in Fig. 3 for D^0 mesons in the interval $4 < p_{\rm T} < 6$ GeV/c with the two-particle cumulants method (a) and D^{*+} mesons in the interval $2 < p_{\rm T} < 4$ GeV/c with the SP method (b). The values of $v_2^{\rm S}$, hereafter indicated as $v_2\{2\}$ and $v_2\{{\rm SP}\}$, are also reported in the figure.

Because the measured D-meson yield has a feed-down contribution from B-meson decays, the measured v_2 is a combination of v_2 of promptly produced and feed-down D mesons. In fact, the contribution of D mesons from B-meson decays is enhanced by the applied selection criteria, because the decay vertices of the feed-down D mesons are, on average, more displaced from the primary vertex. The elliptic flow of promptly produced D mesons, $v_2^{\rm prompt}$, can be obtained from the measured $v_2^{\rm all}$ ($v_2\{{\rm EP}\}$, $v_2\{2\}$ or $v_2\{{\rm SP}\}$) as

$$v_2^{\rm prompt} = \frac{1}{f_{\rm prompt}} v_2^{\rm all} - \frac{1 - f_{\rm prompt}}{f_{\rm prompt}} v_2^{\text{feed-down}}, \quad (8)$$

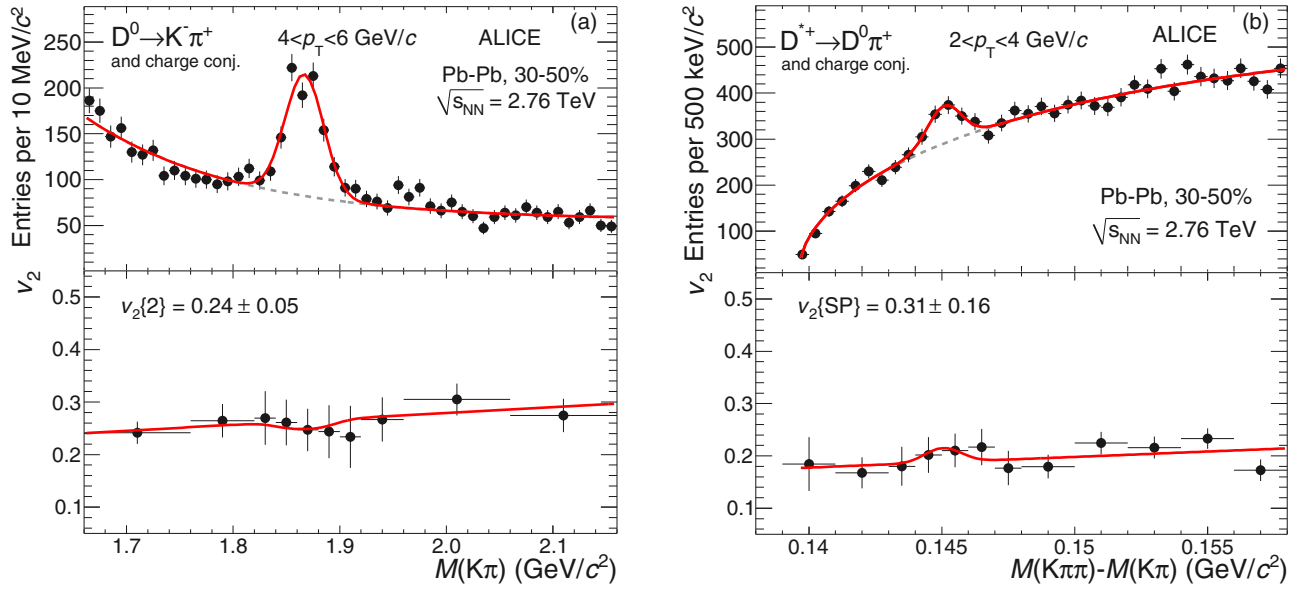

FIG. 3. (Color online) Examples of v_2 extraction with two-particle correlation methods in a selected $p_{\rm T}$ interval for Pb-Pb collisions in the 30%–50% centrality range: the two-particle cumulants method for D^0 (a) and the SP method for D^{*+} (b). The bottom panels report the D-meson v_2 values obtained with the simultaneous fit procedure, as described in the text. The rapidity interval is $|y| < y_{\rm fid}$ (see Sec. III B for details).

where $f_{\rm prompt}$ is the fraction of promptly produced D mesons in the measured raw yield and $v_2^{\rm feed\text{-}down}$ is the elliptic flow of D mesons from B decays, which depends on the dynamics of beauty quarks in the medium. These two quantities have not been measured. According to Eq. (8), the value of $v_2^{\rm all}$ is independent of $f_{\rm prompt}$ and equal to $v_2^{\rm prompt}$, if $v_2^{\rm feed\text{-}down} = v_2^{\rm prompt}$. The central value of the prompt D-meson elliptic flow was defined under this assumption, which removes the need to apply the feed-down correction. Because of the larger mass of the b quark, the v_2 of B mesons is expected to be lower than that of D mesons. Therefore, the choice of $v_2^{\rm feed\text{-}down} = v_2^{\rm prompt}$ as central value is the most conservative for the observation of D meson $v_2 > 0$. The details of the systematic uncertainty related to this assumption are discussed in Sec. IV.

D. Azimuthal dependence of the nuclear modification factor

The in-plane and out-of-plane nuclear modification factors of prompt D^0 mesons are defined as

$$R_{\rm AA}^{\rm in\,(out)}(p_{\rm T}) = \frac{2dN_{\rm AA}^{\rm in\,(out)}/dp_{\rm T}}{\langle T_{\rm AA}\rangle d\sigma_{pp}/dp_{\rm T}}, \tag{9}$$

where $dN_{\rm AA}^{\rm in\,(out)}/dp_{\rm T}$ are the D^0 meson per-event yields, integrated over the two 90°-wide intervals used to determine v_2 with the EP method. The factor 2 in Eq. (9) accounts for the fact that the D-meson yields for Pb-Pb collisions are integrated over half of the full azimuth. $R_{\rm AA}^{\rm in\,(out)}$ was measured in the 30%–50% centrality class for D^0 mesons, which have the highest signal significance, using the yields relative to the EP defined with TPC tracks in $0 < \eta < 0.8$. The average value of the nuclear overlap function in this centrality class, $\langle T_{\rm AA}\rangle = 3.87 \pm 0.18$ mb^{-1}, was determined with the procedure described in Ref. [53].

The yields of prompt D^0 mesons in the two azimuthal intervals were obtained as

$$\left.\frac{dN^{D^0}}{dp_{\rm T}}\right|_{|y|<0.5} = \frac{1}{\Delta y\,\Delta p_{\rm T}} \times \frac{f_{\rm prompt}(p_{\rm T})\frac{1}{2}N_{\rm raw}^{D^0+\overline{D^0}}(p_{\rm T})\Big|_{|y|<y_{\rm fid}}\, c_{\rm refl}(p_{\rm T})}{(\mathrm{Acc}\times\epsilon)_{\rm prompt}(p_{\rm T})\mathrm{BR}N_{\rm events}}. \tag{10}$$

The raw yields $N_{\rm raw}^{D^0+\overline{D^0}}$ were divided by a factor of two to obtain the charge (particle and antiparticle) averaged yields. The factor $c_{\rm refl}(p_{\rm T})$ was introduced to correct the raw yields for the contribution of signal candidates that are present in the invariant mass distribution both as $D^0 \to K^-\pi^+$ and as $\overline{D^0} \to \pi^- K^+$ (the combination with wrong mass hypothesis assignment is called "reflection"). To correct for the contribution of B meson decay feed-down, the raw yields were multiplied by the prompt fraction $f_{\rm prompt}$, whose determination is described later in this section. Furthermore, they were divided by the product of prompt D-meson acceptance and efficiency $(\mathrm{Acc}\times\epsilon)_{\rm prompt}$, normalized by the decay channel branching ratio (BR), the transverse momentum ($\Delta p_{\rm T}$) and rapidity ($\Delta y = 2\,y_{\rm fid}$) interval widths, and the number of events ($N_{\rm events}$). The normalization by Δy gives the corrected yields in one unit of rapidity $|y| < 0.5$.

The $(\mathrm{Acc}\times\epsilon)$ correction was determined, as a function of $p_{\rm T}$, using Monte Carlo simulations with a detailed description of the ALICE detector geometry and the GEANT3 particle transport package [64]. The simulation was tuned to reproduce the (time-dependent) position and width of the interaction vertex distribution, as well as the number of active electronic channels and the accuracy of the detector calibration. The

HIJING v1.383 [65] generator was used to simulate Pb-Pb collisions at $\sqrt{s_{\rm NN}} = 2.76$ TeV and all the produced particles were transported through the detector simulation. Prompt and feed-down D-meson signals were added using pp events from the PYTHIA v6.4.21 [66] event generator with the Perugia-0 tune [67]. Each simulated pp event contained a $c\bar{c}$ or $b\bar{b}$ pair with D mesons decaying into the hadronic channels of interest for the analysis. Of all the particles produced in these PYTHIA pp events, only the heavy-flavor decay products were kept and transported through the detector simulation together with the particles produced by HIJING. To minimize the bias on the detector occupancy, the number of D mesons injected into each HIJING event was adjusted according to the Pb-Pb collision centrality.

The efficiencies were evaluated from simulated events that had the same average charged-particle multiplicity, corresponding to the same detector occupancy, as observed for real events in the centrality class 30%–50%. Figure 4 shows (Acc $\times$ ϵ) for prompt and feed-down D^0 mesons within the rapidity interval $|y| < y_{\rm fid}$. The magnitude of (Acc $\times$ ϵ) increases with $p_{\rm T}$, starting from about 1% and reaching about 10%–15% at high $p_{\rm T}$. Also shown in Fig. 4 are the (Acc $\times$ ϵ) values for the case where no PID was applied. The relative difference with respect to the (Acc $\times$ ϵ) obtained using also the PID selection is only about 5%, thus illustrating the high efficiency of the applied PID criteria. The (Acc $\times$ ϵ) for D mesons from B decays is larger than for prompt D mesons by a factor of about 1.5, because the decay vertices of the feed-down D mesons are more displaced from the primary vertex and are, therefore, more efficiently selected by the analysis cuts.

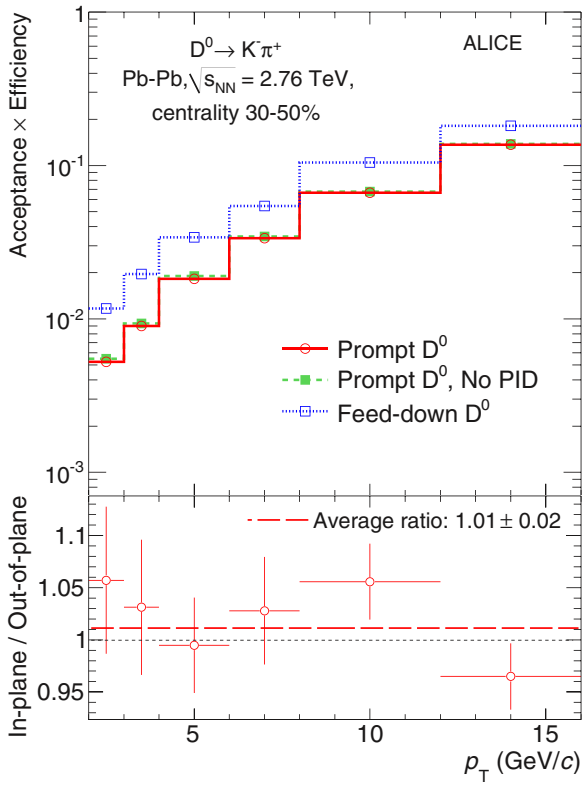

FIG. 4. (Color online) Product of acceptance and efficiency for D^0 mesons in Pb-Pb collisions for 30%–50% centrality class (top panel). The rapidity interval is $|y| < y_{\rm fid}$ (see Sec. III B for details). The values for prompt (solid lines) and feed-down (dotted lines) D^0 mesons are shown. Also displayed, for comparison, are the values for prompt D^0 mesons without PID selection (dashed lines). The bottom panel shows the ratio of the efficiencies for prompt D^0 mesons in the in-plane and out-of-plane regions used for the analysis. This ratio was estimated using simulation samples with a difference in particle multiplicity similar to that observed in data for the two azimuthal regions.

The possible difference in the reconstruction and selection efficiency between in-plane and out-of-plane D^0 mesons was studied using simulations. This difference could arise from the variation of the particle density, and consequently of the detector occupancy, induced by the azimuthal anisotropy of bulk particle production. The difference in occupancy was estimated in data using the multiplicity of SPD tracklets in the two considered azimuthal intervals. Tracklets are defined as combinations of two hits in the two SPD layers that are required to point to the primary vertex. They can be used to measure the multiplicity of charged particles with $p_{\rm T} >$ 50 MeV/c and $|\eta| < 1.6$. The SPD tracklet multiplicity in the 30%–50% centrality class was found to be larger in-plane than out-of-plane by about 12%. To study the efficiency variation, two sets of simulated events with 12% difference in average multiplicity were used. The ratio of the two efficiencies was found to be consistent with unity (see bottom panel of Fig. 4) and therefore no correction was applied.

The correction factor $c_{\rm refl}$ for the contribution of reflections to the raw yield was determined by including in the invariant mass fit procedure a template of the distribution of reflected signal candidates, which was obtained from the simulation for each $p_{\rm T}$ interval. This distribution has a centroid close to the D^0 mass and has typical rms values of about 100 MeV/c^2, i.e., about one order of magnitude larger than the signal invariant mass resolution. The distribution from the simulation was parametrized with the sum of two Gaussians, to remove the statistical fluctuations. In the fit with the template, the ratio of the integrals of the total distribution of reflections and of the Gaussian used for the signal were fixed to the value obtained from the simulation. This ratio is mostly determined by the PID selection, which limits the probability that a true $K^-\pi^+$ pair can be also compatible with the π^-K^+ mass hypothesis. For the v_2 analysis described in the previous section, the PID selection was used only for tracks with $p < 4$ GeV/c. Because the contribution of the reflections does not depend on the angle relative to the EP, it is not necessary to apply the $c_{\rm refl}$ correction for v_2. For the $R_{\rm AA}$ analysis, to minimize the correction, the PID selection was extended to tracks with $p > 4$ GeV/c, requiring the compatibility of the TOF and TPC signals with the expectations for kaons and pions within 3σ. It was verified that this change results in a variation of v_2 well within the uncertainties. The correction factor $c_{\rm refl}$ was determined as the ratio of the signal yield from the fit including the reflections template and the signal yield from the fit without the template. It was computed using the sum of the in-plane and out-of-plane invariant mass distributions, to have a more precise value, and it was applied as in Eq. (10) for both the in-plane and out-of-plane yields. The procedure

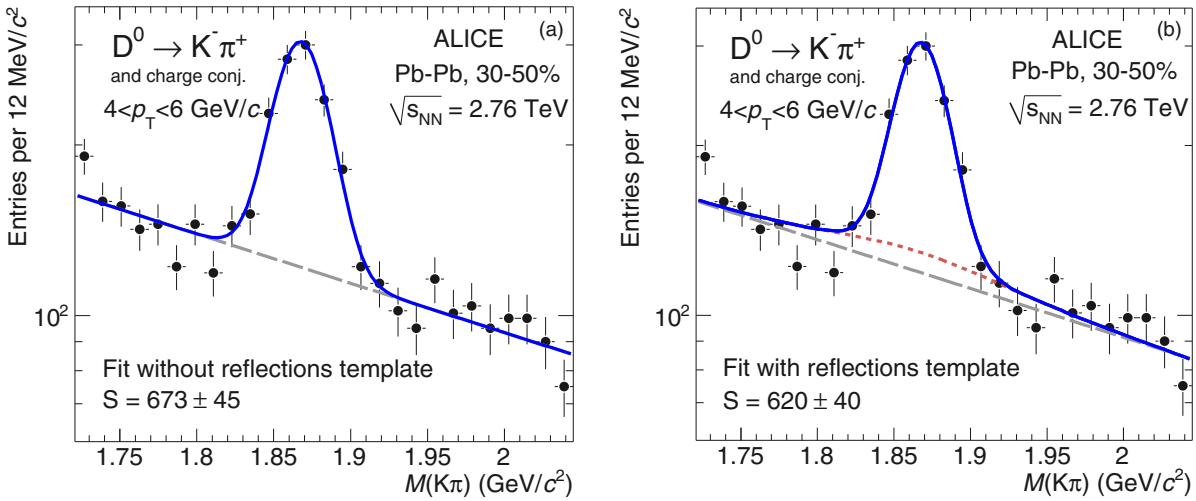

FIG. 5. (Color online) Invariant mass distribution of D^0 candidates with $4 < p_T < 6$ GeV/c in the centrality class 30%–50%: (a) fit without template for reflections and (b) with template for reflections (dotted line). The raw yield obtained as an integral of the signal Gaussian function is reported.

was validated using the simulation, where the signal yield obtained from the fit with the template can be compared with the true signal yield. The numerical value of $c_{\rm refl}$ ranges from 0.98 in the interval $2 < p_T < 3$ GeV/c to 0.90 in the interval $4 < p_T < 16$ GeV/c. Figure 5 shows an example of the fits without (a) and with (b) template for the interval 4–6 GeV/c.

The fraction $f_{\rm prompt}$ of promptly produced D mesons in the measured raw yields was obtained, following the procedure introduced in Ref. [13], as

$$f_{\rm prompt} = 1 - \frac{N_{\rm raw}^{D^0\,\text{feed-down}}}{N_{\rm raw}^{D^0}} = 1 - R_{\rm AA}^{\text{feed-down}} \langle T_{\rm AA} \rangle 2 \left(\frac{d^2\sigma}{dy\,dp_T} \right)_{\text{feed-down}}^{\text{FONLL, EVTGEN}} \times \frac{(\text{Acc} \times \epsilon)_{\text{feed-down}}\, \Delta y\, \Delta p_T \text{BR} N_{\rm evt}}{N_{\rm raw}^{D^0}}. \quad (11)$$

In this expression, where the symbol of the p_T dependence has been omitted for brevity, $N_{\rm raw}^{D^0}$ is the measured raw yield (corrected by the $c_{\rm refl}$ factor) and $N_{\rm raw}^{D^0\,\text{feed-down}}$ is the contribution of D^0 mesons from B decays to the raw yield, estimated on the basis of the FONLL calculation of beauty production [68]. In detail, the B-meson production cross section in pp collisions at $\sqrt{s} = 2.76$ TeV was folded with the $B \to D^0 + X$ decay kinematics using EVTGEN [69] and multiplied by the average nuclear overlap function $\langle T_{\rm AA} \rangle$ in the 30%–50% centrality class, the acceptance-times-efficiency for feed-down D^0 mesons, and the other factors introduced in Eq. (10). In addition, the nuclear modification factor $R_{\rm AA}^{\text{feed-down}}$ of D mesons from B decays was accounted for. The comparison of the $R_{\rm AA}$ of prompt D mesons [70] with that of J/ψ from B decays [71] measured in the CMS experiment indicates that charmed hadrons are more suppressed than beauty hadrons. Therefore, it was assumed that the ratio of the nuclear modification factors for feed-down and prompt D mesons lies in the range $1 < R_{\rm AA}^{\text{feed-down}}/R_{\rm AA}^{\rm prompt} < 3$. The value $R_{\rm AA}^{\text{feed-down}} = 2R_{\rm AA}^{\rm prompt}$ was used to compute the correction, and the variation over the full range, which also accounts for possible centrality and p_T dependencies, was used to assign a systematic uncertainty. The hypothesis on the nuclear modification of feed-down D mesons was changed with respect to the assumption used in Ref. [13], based on the most recent results on the $R_{\rm AA}$ of prompt D meson and nonprompt J/ψ mentioned above. As it was done for the v_2 measurement, the feed-down contribution was computed assuming $v_2^{\text{feed-down}} = v_2^{\rm prompt}$. Therefore, the ratio $R_{\rm AA}^{\text{feed-down}}/R_{\rm AA}^{\rm prompt}$ is the same in-plane and out-of-plane. The systematic uncertainty related to this assumption is discussed in Sec. IV. For D^0 mesons, assuming $R_{\rm AA}^{\text{feed-down}} = 2R_{\rm AA}^{\rm prompt}$, the resulting $f_{\rm prompt}$ ranges from about 0.80 in the lowest transverse-momentum interval ($2 < p_T < 3$GeV/c) to about 0.75 at high p_T.

The D^0 yields in the two azimuthal regions with respect to the EP, obtained from Eq. (10), were corrected for the EP resolution using the correction factor R_2 (Sec. III C) and the relation given in Eq. (4). For example, the correction factor for the in-plane $R_{\rm AA}$ is $(1 + R_2^{-1})/2 + (N^{\rm in}/N^{\rm out})(1 - R_2^{-1})/2$, where $N^{\rm in\,(out)}$ is the D^0 raw yield. The value $R_2 = 0.8059 \pm 0.0001$ for the 30%–50% centrality class and the typical $N^{\rm in}/N^{\rm out}$ magnitude result in a correction of approximately $+4\,(-6)\%$ for the in-plane (out-of-plane) yields.

The prompt D^0 meson production cross section in pp collisions used in the calculation of the nuclear modification factor was obtained by scaling the p_T-differential cross section in $|y| < 0.5$ at $\sqrt{s} = 7$ TeV, measured using a data sample of $L_{\rm int} = 5$ nb^{-1} [55]. The p_T-dependent scaling factor was defined as the ratio of the cross sections obtained from FONLL calculations [68] at $\sqrt{s} = 2.76$ and 7 TeV [72]. The scaled D^0 meson p_T-differential cross section is consistent with that measured at $\sqrt{s} = 2.76$ TeV using a smaller statistics data sample with $L_{\rm int} = 1.1$ nb^{-1} [56], which only covered a

TABLE II. Systematic uncertainties on the measurement of v_2 in the 30%–50% centrality class for the interval $4 < p_T < 6$ GeV/c. The uncertainties are comparable in the other p_T intervals.

Particle v_2 analysis	D^0			D^+			D^{*+}		
	v_2{EP}	v_2{SP}	v_2{2}	v_2{EP}	v_2{SP}	v_2{2}	v_2{EP}	v_2{SP}	v_2{2}
M and v_2 fit stability (%)	9	10	8	25	8	17	30	14	11
Two or three subevents R_2 (%)	2.3	–	–	2.3	–	–	2.3	–	–
R_2 centrality dependence (%)	2	–	–	2	–	–	2	–	–
Centrality selection (%)	–	10	10	–	10	10	–	10	10
Total (excluding B feed-down) (%)	9	14	13	25	13	20	30	17	15
B feed-down (%)		$^{+48}_{-0}$			$^{+26}_{-0}$			$^{+26}_{-0}$	

reduced p_T interval with a statistical uncertainty of 20%–25% and was therefore not used as a pp reference. The correction for reflections was not applied for the D^0 cross section in pp collisions. It was verified that the resulting signal bias is smaller than 5% ($c_{\text{refl}} > 0.95$), which is less than the systematic uncertainty assigned for the yield extraction (10%–20% [55]).

IV. SYSTEMATIC UNCERTAINTIES

Several sources of systematic uncertainty were considered for both v_2 and R_{AA} analyses. The uncertainties on v_2 are described first. Afterwards, the systematic uncertainties affecting R_{AA} in plane and out of plane are discussed. The uncertainties for the 30%–50% centrality class are summarized in Tables II and III. In the following, the quoted uncertainties are symmetric around the central value of the measurement, unless the upper and lower parts are reported separately.

A. Uncertainties on v_2

One of the main sources of uncertainty originates from the D-meson yield extraction using a fit to the invariant mass distributions. This uncertainty was estimated by repeating the fits under different conditions and by utilizing alternative methods for the yield determination. For the v_2 analysis with the EP method, the fit ranges and the functional forms for the combinatorial background were varied. Polynomial and exponential functions were tried for D^0 and D^+ background shapes, while a threshold function multiplied by an exponential was considered for the D^{*+}: $a\sqrt{\Delta M - m_\pi}e^{b(\Delta M - m_\pi)}$, with a and b as free parameters. The D-meson yield was also extracted by counting the entries in the invariant mass distributions after background subtraction. For this procedure the background was estimated with a fit to the left and right sides of the D-meson invariant mass peak (sideband regions), using the fit functions described in Sec. III B. The v_2 analysis employing the EP method was performed by fixing the Gaussian centroids and widths of the in-plane and out-of-plane invariant mass distributions to the values obtained from a fit of the φ-integrated distribution. The analysis was repeated with free Gaussian parameters in the fit. The systematic uncertainty owing to the yield measurement was estimated as the maximum variation of the v_2 values obtained from the described tests. It amounts to 10%–20% for the D^0 meson, depending on the p_T and centrality intervals, and 20%–50% for the D^+ and D^{*+} mesons, depending on the p_T interval. The same procedure was applied for the two-particle correlation methods (SP and two-particle cumulants), except for the bin counting method and the fixed Gaussian centroids and widths. Instead, the parametrization of the background $v_2^B(M)$ was varied from a first-order to a second-order polynomial. The resulting uncertainty is in the range 15%–30%.

For the EP method, two alternative procedures were considered to extract v_2, which are not directly based on the measurement of the signal yields from the invariant mass distribution. These procedures use the distribution of $\cos(2\Delta\varphi)$ versus invariant mass (where $\Delta\varphi = \varphi_D - \psi_2$) and the relation $v_2 = \langle\cos(2\Delta\varphi)\rangle$. In the first procedure, the distribution of $\cos(2\Delta\varphi)$ is considered for the signal region ($|M - m_D| <$

TABLE III. Systematic uncertainties on the measurement of the D^0 meson R_{AA} in plane and out of plane in the 30%–50% centrality class for two p_T intervals. The uncertainties are grouped according to the type of correlation between the in-plane and out-of-plane cases.

p_T interval (GeV/c)	2–3	12–16
Uncorrelated uncertainties		
Yield extraction (%)	7	10
Total uncorrelated (%)	7	10
Correlated uncertainties		
Correction for reflections (%)	1	5
Tracking efficiency (%)	10	10
Cut efficiency (%)	10	10
PID efficiency (%)	5	5
D^0 p_T distribution in MC (%)	2	0
pp reference (%)	$^{+20}_{-35}$	18
Data syst. (%)	17	17
$\sqrt{s}$ scaling (%)	$^{+10}_{-31}$	$^{+5}_{-6}$
B feed-down yield (%)	$^{+9}_{-13}$	$^{+14}_{-12}$
Total correlated (%)	$^{+22}_{-37}$	$^{+28}_{-27}$
Normalization uncertainties		
pp cross section norm. (%)	3.5	
$\langle T_{AA}\rangle$ (%)	4.7	
Centrality class definition (%)	2	
Total normalization (%)	6.2	
Anticorrelated uncertainties		
Uncertainty on R_2 (%)	0.5	0.5
B feed-down v_2 (%)	in: $^{+4}_{-0}$; out: $^{+0}_{-6}$	in: $^{+7}_{-0}$; out: $^{+0}_{-5}$
Total anticorrelated (%)	in: $^{+4}_{-0.5}$; out: $^{+0.5}_{-6}$	in: $^{+7}_{-0.5}$; out: $^{+0.5}_{-5}$

3σ) and the two sideband regions ($4 < |M - m_{\rm D}| < 7\sigma$). The distribution of $\cos(2\Delta\varphi)$ for the background is obtained by averaging, bin by bin, the distributions of $\cos(2\Delta\varphi)$ in the two sidebands. This background distribution is then rescaled to the integral of the background fit function in the invariant mass signal region and it is subtracted from the total $\cos(2\Delta\varphi)$ distribution in the signal region. In this way, the distribution of $\cos(2\Delta\varphi)$ of the signal is obtained. Its mean value gives the D-meson v_2. In the second procedure, a distribution of $\langle\cos(2\Delta\varphi)\rangle$ as a function of invariant mass is used for a simultaneous fit of the v_2 and the yield, as in the case of the two-particle correlation methods. These two alternative procedures result in D-meson v_2 values that are consistent with those obtained from the EP method with two $\Delta\varphi$ bins. Therefore, no systematic uncertainty is taken for the v_2 extraction procedure.

The v_2 analysis was repeated with different sets of cuts for the selection of D-meson candidates. A set of tighter and a set of looser cuts with respect to those described in Sec. III B were considered for each D-meson species, thus varying the signal yield by about 30%–50% and, consequently, the significance and the signal-to-background ratio. The resulting v_2 values were found to be consistent within statistical uncertainties. Consequently, this contribution to the systematic uncertainty was neglected.

The uncertainty owing to the EP resolution was estimated with the two- and three-subevent methods with an η gap. The three subevents were defined using the TPC tracks and the signals in the two VZERO detectors. The resolutions estimated with these two methods differ by 6.9%, 2.0%, and 2.3% in the 0%–10%, 10%–30%, and 30%–50% centrality classes, respectively [see Fig. 1(b)]. A symmetric systematic uncertainty equal to the relative difference between R_2 values obtained with the two- and three-subevent methods was assigned to the D-meson v_2.

The uncertainty owing to the centrality dependence of the EP resolution was estimated from the difference between two ways to define the average resolution in the centrality classes used in the analysis, starting from the resolutions in fine centrality intervals [see Fig. 1(b)], namely, a plain arithmetic average and an average weighted with the D-meson yield measured in smaller centrality classes (2.5% wide). The latter was estimated using D^0 meson raw yields in wide $p_{\rm T}$ intervals and the sum of the two $\Delta\varphi$ intervals, to reduce the statistical fluctuations. The difference between these averages was found to be about 2%, 0.5%, and 2% for the 0%–10%, 10%–30%, and 30%–50% centrality classes, respectively. The resulting total uncertainties on R_2 amount to 7%, 2%, and 3% for the three centrality classes.

The distribution of collision impact parameters selected in a given centrality class slightly depends on the pseudorapidity coverage of the detector used for the centrality determination. The analysis was repeated using the number of tracks in the TPC as a centrality estimator, instead of the total signal measured in the VZERO detector. A relative systematic uncertainty of 10% was assigned to the v_2 values measured with the SP and two-particle cumulant methods, on the basis of the difference of the resulting v_2 values. This difference could originate from the dependence of the RFP multiplicity fluctuations on the centrality estimator. No significant difference was observed for the EP method when using the TPC, instead of the VZERO, for the centrality determination.

As explained at the end of Sec. III C, the central value of the prompt D-meson v_2 was obtained without applying a correction for the feed-down from B-meson decays, on the basis of the assumption $v_2^{\text{feed-down}} = v_2^{\text{prompt}}$ [see Eq. (8)]. The systematic uncertainty associated with this assumption was estimated by varying it in the interval $0 \leqslant v_2^{\text{feed-down}} \leqslant v_2^{\text{prompt}}$. This range covers all model predictions for v_2 of charm and beauty hadrons [20,21,42]. The lower limit of the variation range, $v_2^{\text{feed-down}} = 0$, gives $v_2^{\text{prompt}} = v_2^{\text{all}}/f_{\text{prompt}}$. The f_{prompt} values for each of the D-meson species and each $p_{\rm T}$ interval were obtained using FONLL calculations [68] (see Sec. III D). Under the assumption $R_{\rm AA}^{\text{feed-down}} = 2R_{\rm AA}^{\text{prompt}}$, the f_{prompt} values change from 0.8 to 0.75 (0.85 to 0.8) from low to high $p_{\rm T}$ for D^0 (D^+ and D^{*+}) mesons (the feed-down contribution is larger for D^0 mesons because of the stronger constraint on the separation between the secondary and the primary vertex). A set of f_{prompt} values was computed by varying the heavy-quark masses and the perturbative scales in the FONLL calculation as prescribed in Ref. [68], and the ratio $R_{\rm AA}^{\text{feed-down}}/R_{\rm AA}^{\text{prompt}}$ in the range $1 < R_{\rm AA}^{\text{feed-down}}/R_{\rm AA}^{\text{prompt}} < 3$. The smallest value of f_{prompt} was used to assign the uncertainty related to the B feed-down contribution to the elliptic flow of prompt D mesons. The maximum relative uncertainty is about $^{+45}_{-0}$%.

B. Uncertainties on $R_{\rm AA}$

For the analysis of the D^0-meson $R_{\rm AA}$ in-plane and out-of-plane, the same sources of systematic uncertainty as for the v_2 measurement with the EP method were considered. Additional systematic uncertainties, which are specific to the $R_{\rm AA}$ measurement, stem from the tracking, selection, and PID efficiencies, and from the uncertainty of the proton-proton reference yield. The evaluation of these uncertainties is similar as in Ref. [13] and it is described in the following.

To reduce the statistical fluctuations, the uncertainty of the D^0 yield extraction was estimated using the φ-integrated invariant mass distributions. The fit procedure was varied, as described for the v_2 analysis. The resulting uncertainty is 7% for $2 < p_{\rm T} < 8$ GeV/c and 10% for $8 < p_{\rm T} < 16$ GeV/c. The systematic uncertainty on the correction factor for signal reflections, $c_{\rm refl}$, was estimated by changing by $\pm 50\%$ the ratio of the integral of the reflections over the integral of the signal obtained from the simulation and used in the invariant mass fit with the reflections template. In addition, the shape of the reflections template was varied using a polynomial parametrization of the distribution from the simulation, instead of a double-Gaussian parametrization. These variations resulted in an uncertainty of 1%–2% for $2 < p_{\rm T} < 4$ GeV/c and of 5% for $4 < p_{\rm T} < 16$ GeV/c on the $c_{\rm refl}$ factor.

The systematic uncertainty of the tracking efficiency was estimated by comparing the probability to match the TPC tracks extrapolated to the ITS hits in data and simulation and by varying the track quality selection criteria (for example, the minimum number of associated hits in the TPC and in the ITS and maximum χ^2/ndf of the momentum fit). The efficiency of

the track matching and the association of hits in the silicon pixel layers was found to be described by the simulation with maximal deviations on the level of 5% in the $p_{\rm T}$ range relevant for this analysis (0.5–15 GeV/c). The effect of misassociating ITS hits to tracks was studied using simulations. It was found that the fraction of D mesons with at least one decay track with a wrong hit associated increases with centrality, owing to the higher detector occupancy, and vanishes at high $p_{\rm T}$, where the track extrapolation between ITS layers is more precise. In the centrality class 30%–50%, this fraction is about 2% in the transverse-momentum interval $2 < p_{\rm T} < 16$ GeV/c. It was verified that the signal selection efficiencies are the same for D mesons with and without wrong hit associations. The total systematic uncertainty of the track reconstruction procedure amounts to 5% for single tracks, which results in a 10% uncertainty for D^0 mesons (two-track final state).

The uncertainty of the correction for the selection on the decay topology was evaluated by repeating the analysis with different sets of cuts and was defined as the variation of the resulting corrected yields with respect to the value corresponding to the baseline cuts. This resulted in a variation up to 10% in the $p_{\rm T}$ intervals used in the analysis. The analysis was repeated without applying the PID selection and the resulting corrected yields were found to be consistent within 5% with those obtained with the PID selection. Therefore, a systematic uncertainty of 5% was assigned for the PID efficiency correction in the simulation.

The uncertainty of the efficiencies arising from the difference between the real and simulated D-meson momentum distributions depends on the width of the $p_{\rm T}$ intervals and on the variation of the efficiencies within them. This uncertainty includes also the effect of the $p_{\rm T}$ dependence of the nuclear modification factor. The mean efficiency in a given $p_{\rm T}$ interval was computed by reweighting the simulated D^0 meson yield according to the $p_{\rm T}$ distribution measured for D^0 mesons in central Pb-Pb collisions [13]. The systematic uncertainty was defined as the difference with respect to the efficiency computed using the $p_{\rm T}$ distribution from a FONLL calculation [68] multiplied by the $R_{\rm AA}$ value from one of the models [21] that closely describe the central value of the measurement (see Sec. VI). This uncertainty is of 2% in the interval $2 < p_{\rm T} < 3$ GeV/c, where the efficiency increases steeply with $p_{\rm T}$ and below 1% for $p_{\rm T} > 3$ GeV/c.

The uncertainty of 3% on the EP resolution correction factor R_2 in the 30%–50% centrality class was propagated to the $R_{\rm AA}$ observables, resulting in an uncertainty in the range 0.5%–2%, depending on the $p_{\rm T}$ interval.

The systematic uncertainty owing to the subtraction of feed-down D mesons from B-meson decays was estimated following the procedure described in Ref. [13]. The contribution of the uncertainties inherent in the FONLL perturbative calculation was included by varying the heavy-quark masses and the factorization and renormalization scales in the ranges proposed in Ref. [68]. This contribution partly cancels in the $R_{\rm AA}$ ratio, because these variations are done simultaneously for the Pb-Pb yield and for the pp reference cross section. The uncertainty introduced by the hypothesis on the value of the feed-down D-meson $R_{\rm AA}$ was estimated from the variation $1 < R_{\rm AA}^{\text{feed-down}}/R_{\rm AA}^{\text{prompt}} < 3$. The total uncertainty owing to the feed-down correction, which is common to the in-plane and out-of-plane $R_{\rm AA}$, ranges between $^{+9}_{-13}$% at low $p_{\rm T}$ and $^{+14}_{-12}$% at high $p_{\rm T}$. The hypothesis on the value of v_2 for D mesons from B decays, that was varied in the range $0 \leqslant v_2^{\text{feed-down}} \leqslant v_2^{\text{prompt}}$, introduces an additional contribution to the systematic uncertainty, which is anticorrelated between $R_{\rm AA}^{\text{in-plane}}$ and $R_{\rm AA}^{\text{out-of-plane}}$. This uncertainty is typically of $^{+5}_{-0}$% for in plane and $^{+0}_{-5}$% for out of plane.

The uncertainty of the pp reference used for the calculation of $R_{\rm AA}$ has two contributions. The first is attributable to the systematic uncertainty of the measured D^0 meson $p_{\rm T}$-differential yield at $\sqrt{s} = 7$ TeV and it is about 17%, approximately constant with $p_{\rm T}$ [55]. The second contribution is attributable to the scaling to $\sqrt{s} = 2.76$ TeV. It ranges from $^{+31}_{-10}$% at low $p_{\rm T}$ to about 5% at high $p_{\rm T}$ [13].

The uncertainties on the pp cross section normalization (3.5%) [55] and the average nuclear overlap function $\langle T_{\rm AA}\rangle$ (4.7% for the class 30%–50%) were also included. The contribution owing to the 1.1% relative uncertainty on the fraction of the hadronic cross section used in the Glauber fit to determine the centrality classes [53] was obtained by estimating the variation of the D-meson $dN/dp_{\rm T}$ when the limits of the centrality classes are shifted by ±1.1% (e.g., instead of 30%–50%, 30.3%–50.6%, and 29.7%–49.5%) [13]. The resulting uncertainty, common to all $p_{\rm T}$ intervals, is 2% for the 30%–50% centrality class. The total normalization uncertainty, computed taking the quadratic sum of these three contributions, is 6.2%.

The systematic uncertainties of $R_{\rm AA}$ were grouped into three categories, depending on their correlation between the in-plane and the out-of-plane measurements. The uncorrelated systematic uncertainties affect the two $R_{\rm AA}$ independently; this category includes only the yield extraction uncertainty. The correlated systematic uncertainties affect the two $R_{\rm AA}$ in the same way and do not affect their relative difference. The uncertainties on the correction efficiencies (for track reconstruction, selection cuts, PID, and D^0 $p_{\rm T}$ distribution in the simulation) and on the correction for reflections, as well as those on the pp reference, the variation of perturbative scales and the $R_{\rm AA}^{\text{feed-down}}$ hypothesis used for the feed-down subtraction are included in this category. Another correlated uncertainty is attributable to the normalization ($\langle T_{\rm AA}\rangle$ and centrality class definition), which is quoted separately. The anticorrelated systematic uncertainties could shift the two $R_{\rm AA}$'s in opposite directions, affecting their difference. This category includes the contribution from the unknown azimuthal anisotropy of feed-down D mesons (variation of $v_2^{\text{feed-down}}$) and the contribution from the EP resolution correction factor. Within each category, the uncertainties from different sources were added in quadrature.

V. RESULTS

A. Elliptic flow

The elliptic flow v_2 measured with the EP method is shown as a function of $p_{\rm T}$ in the left column of Fig. 6 for D^0, D^+, and D^{*+} mesons in the 30%–50% centrality class. The EP

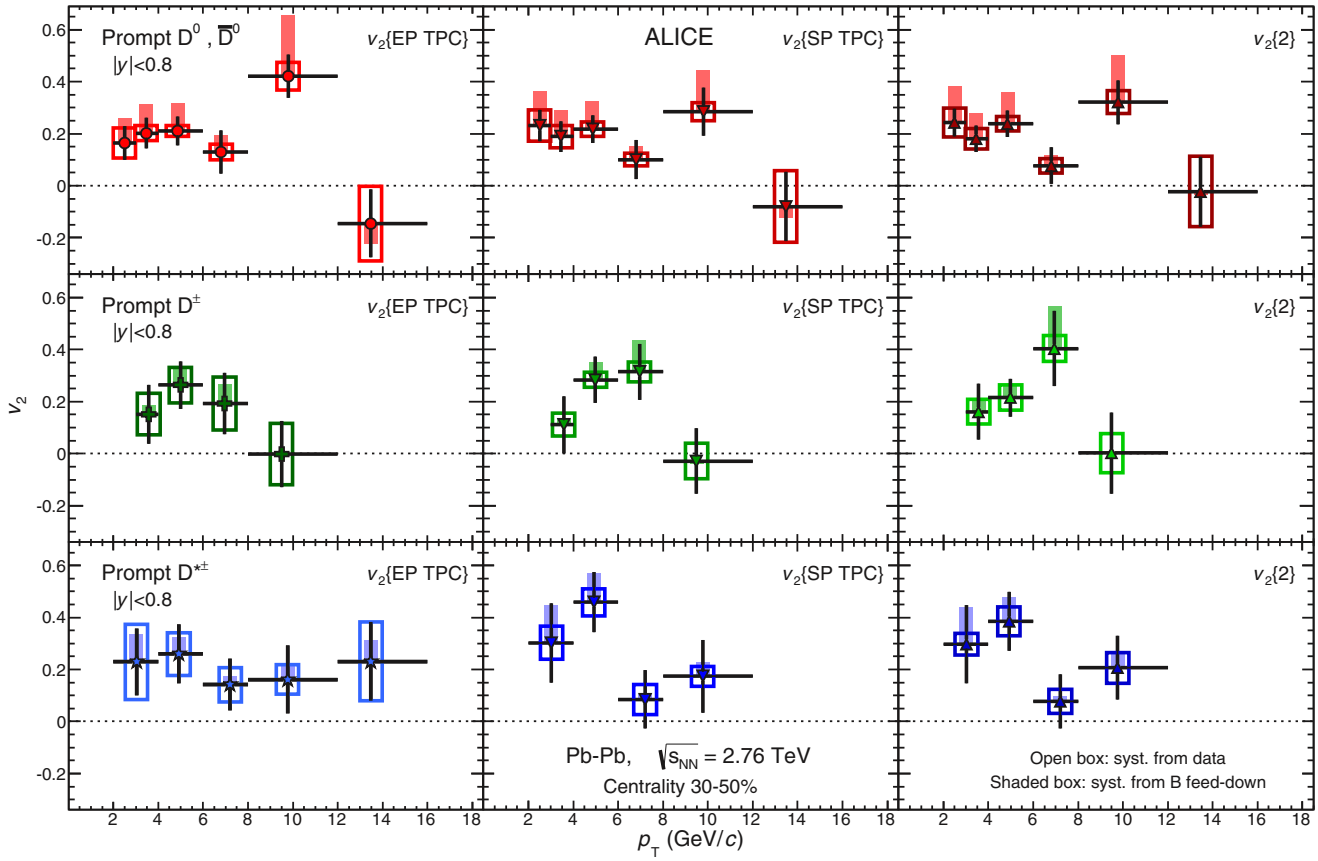

FIG. 6. (Color online) v_2 as a function of p_T in the 30%–50% centrality class, for D^0, D^+, and D^{*+} mesons (rows) with the EP (from Ref. [46]), SP, and two-particle cumulant methods (columns). For the first method, the EP was estimated with TPC tracks in $0 < \eta < 0.8$; for the other methods, TPC tracks in $-0.8 < \eta < 0.8$ were used as RFPs. The symbols are positioned at the average p_T measured within each interval.

was estimated from TPC tracks in the range $0 < \eta < 0.8$. The symbols are positioned horizontally at the average p_T of reconstructed D mesons. This value was determined as the average of the p_T distribution of candidates in the signal-invariant mass region, after subtracting the contribution of the background candidates, which was estimated from the side bands. This average p_T of the reconstructed D mesons is larger than that of the produced D mesons, because the efficiency increases with increasing p_T (see Fig. 4). The vertical error bars represent the statistical uncertainty, the open boxes are the systematic uncertainties from the anisotropy determination and the EP resolution, and the solid boxes are the uncertainties owing to the B feed-down contribution. The elliptic flow of the three D-meson species is consistent within statistical uncertainties and ranges between 0.1 and 0.3 in the interval $2 < p_T < 8$ GeV/c. For $p_T > 12$ GeV/c, v_2 is consistent with zero within the large statistical uncertainties. The central and rightmost panels of the same figure show the v_2 results obtained with the SP and two-particle cumulant methods, respectively. The results from the three methods are consistent within statistical uncertainties for the three meson species.

Figure 7 shows the v_2 of the D^0 mesons measured with the EP (a) and SP (b) methods using RFPs from the TPC detector (i.e., in a η range that overlaps with the D-meson acceptance) or from the VZERO detectors at $-3.7 < \eta < -1.7$ and $2.8 < \eta < 5.1$ (i.e., with a large η gap with respect to the D mesons). The agreement between the results with and without η gap indicates that the bias owing to nonflow correlations is within the statistical precision of the measurement.

For the 30%–50% centrality class an average v_2 of D^0, D^+, and D^{*+} was already computed in Ref. [46] from the EP method results, using the statistical uncertainties as weights. The resulting D-meson v_2 has a value $0.204 \pm 0.030\,(\text{stat}) \pm 0.020\,(\text{syst})\,^{+0.092}_{-0}\,(B\text{ feed-down})$, averaged over the p_T intervals 2–3, 3–4, 4–6 GeV/c. This value is larger than zero with a significance, calculated from the combined statistical and systematic uncertainties, of 5.7σ.

Figure 8 shows the D^0 meson v_2 in the three centrality classes 0%–10%, 10%–30%, and 30%–50% as a function of p_T. The D^0 meson v_2 is compared with that of charged particles [33] for the same centrality classes. D-meson and charged-particle results are obtained with the EP method using TPC and the VZERO detectors, respectively. The magnitude of v_2 is similar for charmed hadrons and light-flavor hadrons, which dominate the charged-particle sample.

The centrality dependence of the D^0 elliptic flow is shown in Fig. 9 for three transverse-momentum intervals in the range $2 < p_T < 6$ GeV/c. A decreasing trend of v_2 towards more

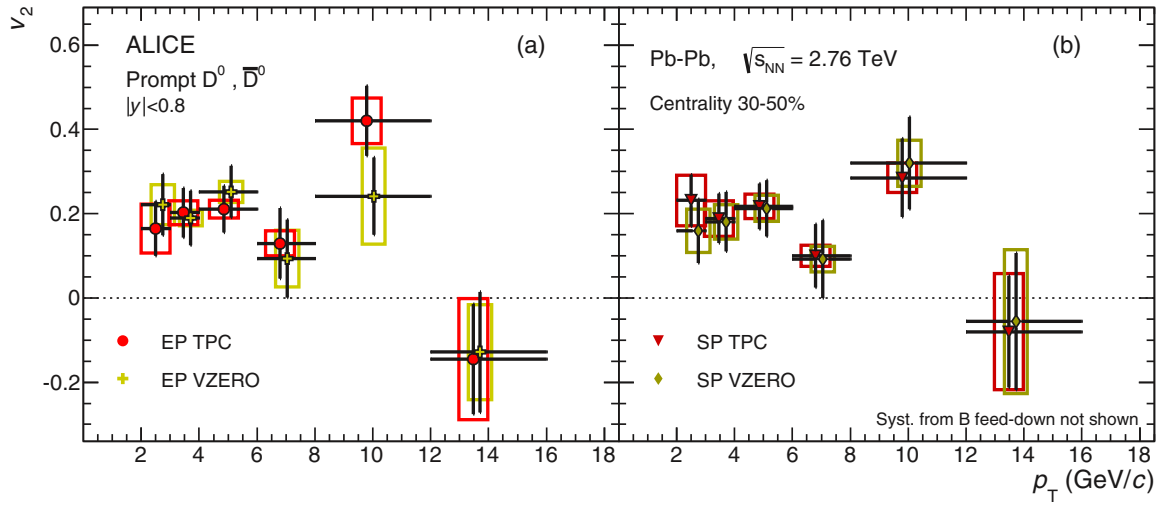

FIG. 7. (Color online) D^0 meson v_2 as a function of p_T in the 30%–50% centrality class, with the RFPs from the TPC or from the VZERO detectors ($-3.7 < \eta < -1.7$ and $2.8 < \eta < 5.1$). (a) Event-plane method. (b) Scalar-product method. For visibility, the symbols for the VZERO case are slightly displaced horizontally.

central collisions is observed, as expected because of the decreasing initial geometrical anisotropy.

B. Nuclear modification factor in and out of the event plane

The nuclear modification factors of D^0 mesons in the 30%–50% centrality class are shown in Fig. 10 for the in-plane and out-of-plane directions with respect to the EP. The EP was estimated with TPC tracks in $0 < \eta < 0.8$. The error bars represent the statistical uncertainties, which are to a large extent independent for the two azimuthal intervals, because they are dominated by the statistical uncertainties of the Pb-Pb data. The uncorrelated (empty boxes), correlated (brackets), and anticorrelated (shaded boxes) systematic uncertainties are shown separately. The normalization uncertainty, shown as a box at $R_{AA} = 1$, is common to both measurements.

A large suppression is observed in both directions with respect to the EP for $p_T > 4$ GeV/c. At lower transverse momentum, the suppression appears to be reduced, especially in the in-plane direction, where R_{AA} reaches unity at a p_T of 2–3 GeV/c. Overall, a stronger suppression in the out-of-plane direction is observed. The ordering $R_{AA}^{\text{out-of-plane}} < R_{AA}^{\text{in-plane}}$ is

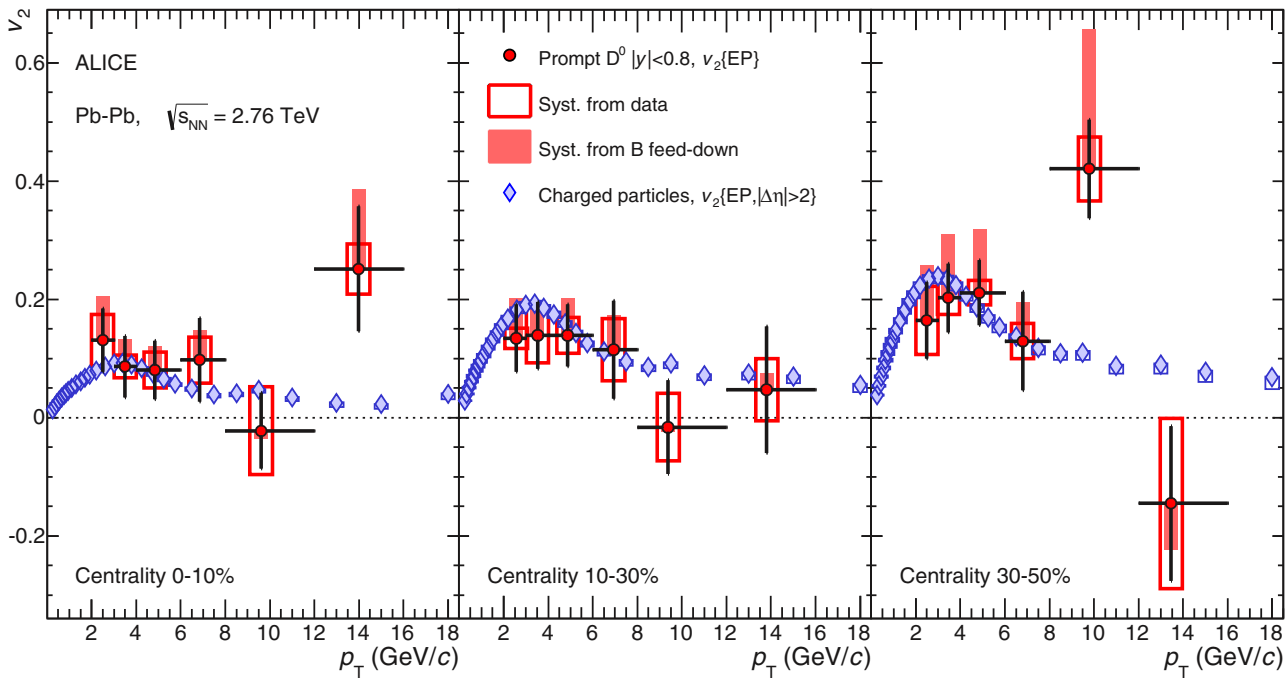

FIG. 8. (Color online) Comparison of prompt D^0 meson and charged-particle v_2 [33] in three centrality classes as a function of p_T. Both measurements are done with the EP method. For charged particles a gap of two η units is used.

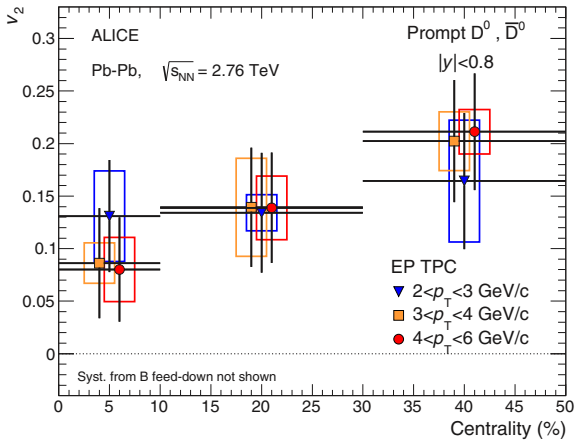

FIG. 9. (Color online) D^0 meson v_2 with EP method in three p_T intervals as a function of centrality. For visibility, the points are displaced horizontally for two of the p_T intervals.

equivalent to the observation of $v_2 > 0$ (as shown in the top-left panel of Fig. 6), because Eq. (4) can be expressed also as

$$v_2 = \frac{\pi}{4}\frac{R_{AA}^{\text{in-plane}} - R_{AA}^{\text{out-of-plane}}}{R_{AA}^{\text{in-plane}} + R_{AA}^{\text{out-of-plane}}}. \quad (12)$$

VI. COMPARISON WITH MODEL CALCULATIONS

A number of theoretical model calculations are available for the elliptic flow coefficient v_2 and the nuclear modification factor R_{AA} of heavy-flavor hadrons. Figure 11 shows a comprehensive comparison of these models to measurements of the R_{AA} of D^0 mesons in plane and out of plane in the 30%–50% centrality class, of the average R_{AA} of D^0, D^+, and D^{*+} in the 0%–20% centrality class [13], and of the v_2 averaged over the D-meson species in the centrality class 30%–50% [46].

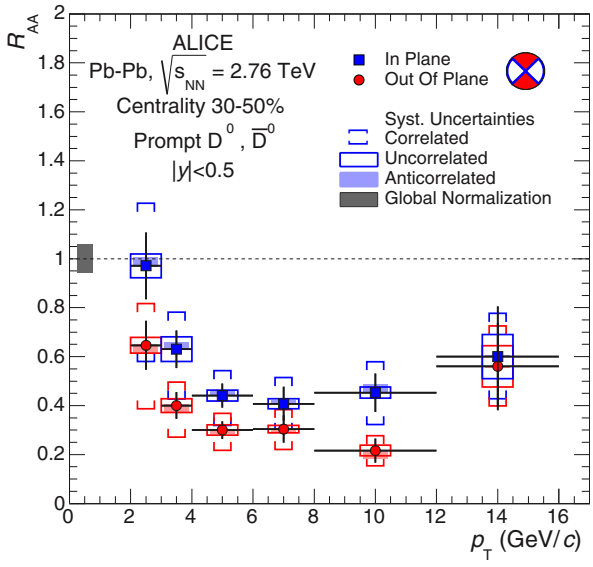

FIG. 10. (Color online) Nuclear modification factor R_{AA} of D^0 mesons in the 30%–50% centrality class in two 90°-wide azimuthal intervals centered on the in-plane and on the out-of-plane directions. The correlated, uncorrelated, and anticorrelated contributions to the systematic uncertainty are shown separately.

The following models are considered and compared to data:

(i) *WHDG [18].* This is a perturbative QCD (pQCD) calculation of parton energy loss, including both radiative (DGLV [73]) and collisional processes. A realistic collision geometry based on the Glauber model [9] is used, without hydrodynamical expansion, so that the anisotropy results only from path-length-dependent energy loss. Hadronization is performed using vacuum fragmentation functions. The medium density is constrained on the basis of the π^0 R_{AA} in central collisions at $\sqrt{s_{NN}} = 200$ GeV and scaled to LHC energy according to the increase of the charged-particle multiplicity. The model describes well the D-meson R_{AA} in the centrality interval 0%–20% (slightly overestimating the suppression, as it does also for charged particles [13]), and gives an almost p_T-independent $v_2 \approx 0.06$, which is smaller than the measured values in the range $2 < p_T < 6$ GeV/c. Consequently, the difference between the in-plane and out-of-plane R_{AA} suppression is underestimated: The model describes well the out-of-plane R_{AA} and lies below the in-plane R_{AA}.

(ii) *MC@sHQ+EPOS, Coll+Rad(LPM) [74].* This pQCD model includes collisional and radiative (with Landau-Pomeranchuk-Migdal correction [75]) energy-loss mechanisms for heavy quarks by running a strong coupling constant. The medium fluid dynamical expansion is based on the EPOS model [76]. A component of recombination of heavy quarks with light-flavor quarks from the QGP is also incorporated in the model. This model yields a substantial anisotropy ($v_2 \approx 0.12$–0.08 from low to high p_T), which is close to that observed in data. The nuclear modification factor is substantially overestimated below $p_T \approx 5$ GeV/c and correctly described at higher p_T.

(iii) *TAMU elastic [43].* This is a heavy-flavor transport model based on collisional, elastic processes only. The heavy-quark transport coefficient is calculated within a nonperturbative T-matrix approach, where the interactions proceed via resonance formation that transfers momentum from the heavy quarks to the medium constituents. The model includes hydrodynamic medium evolution, constrained by light-flavor hadron spectra and elliptic flow data, and a component of recombination of heavy quarks with light-flavor quarks from the QGP. Diffusion of heavy-flavor hadrons in the hadronic phase is also included. The model provides a good description of the observed suppression of D mesons over the entire p_T range. The maximum anisotropy, v_2 of about 0.13 at $2 < p_T < 4$GeV/c, is close to that observed in the data. Towards larger p_T, the model tends to underestimate v_2, as well as the difference of the in-plane and the out-of-plane R_{AA}.

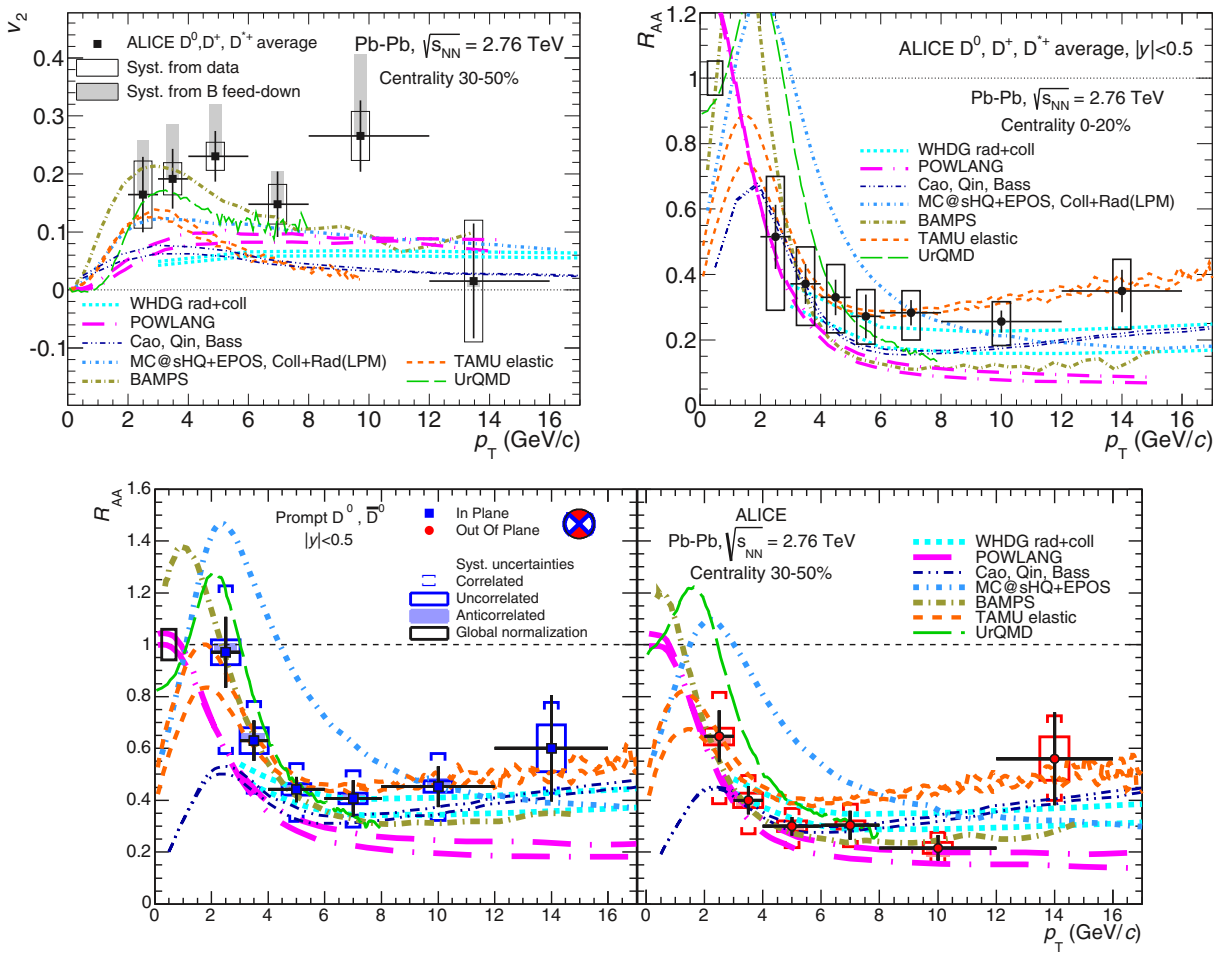

FIG. 11. (Color online) Model comparisons for average D-meson v_2 in the 30%–50% centrality class (top left), average D-meson R_{AA} in the 0%–20% centrality class (top right) [13], D^0 R_{AA} in plane and out of plane in the 30%–50% centrality class (bottom panels). The seven model calculations are described in the text: WHDG rad+coll [18], POWLANG [19], Cao, Qin, Bass [45], MC@sHQ+EPOS, Coll+Rad(LPM) [74], BAMPS [21], TAMU elastic [43], UrQMD [44]. The models WHDG rad+coll, POWLANG, TAMU elastic, and UrQMD are shown by two lines that represent their uncertainty.

(iv) *POWLANG [19].* This transport model is based on collisional processes treated within the framework of Langevin dynamics, within an expanding deconfined medium described by relativistic viscous hydrodynamics. The transport coefficients entering into the relativistic Langevin equation are evaluated by matching the hard-thermal-loop calculation of soft collisions with a perturbative QCD calculation for hard scatterings. Hadronization is implemented via vacuum fragmentation functions. This model overestimates the high-p_T suppression, yields a value for v_2 significantly smaller than observed in data, and also underestimates the difference between the in-plane and the out-of-plane suppression.

(v) *BAMPS [21].* This partonic transport model is based on the Boltzmann approach to multiparton scattering. Heavy quarks interact with the medium via collisional processes computed using a running value of the strong-coupling constant. Hadronization is performed using vacuum fragmentation functions. The lack of radiative processes is accounted for by scaling the binary cross section with a correction factor, which is tuned to describe the heavy-flavor decay electron elliptic flow and nuclear modification factor at RHIC. When applied to calculations for LHC energy, this correction factor results in an underestimation of the D-meson R_{AA} for $p_T > 5$ GeV/c and a large azimuthal anisotropy, with v_2 values up to 0.20, similar to those observed in the data. The nuclear modification factors in plane and out of plane are well described up to 5 GeV/c, while for higher p_T the in-plane R_{AA} is underestimated.

(vi) *UrQMD [44].* The Langevin approach for the transport of heavy quarks is in this case implemented within the UrQMD model [77]. This model includes a realistic description of the medium evolution by combining hadronic transport and ideal hydrodynamics. The transport of heavy quarks is calculated on the basis of a resonance model with a decoupling temperature of 130 MeV. Hadronization via quark

coalescence is included. The calculation parameters are tuned to reproduce the heavy-flavor measurements at RHIC ($\sqrt{s_{\rm NN}} = 200$ GeV) and kept unchanged for calculations at the LHC energy. The model describes the measured D-meson v_2, as well as $R_{\rm AA}$ in the interval $4 < p_{\rm T} < 8$ GeV/c, but it fails to reproduce the significant suppression measured for $R_{\rm AA}$ at $p_{\rm T}$ of 2–3 GeV/c.

(vii) *Cao, Qin, Bass [45].* This model is also based on the Langevin approach. In addition to quasielastic scatterings, radiative energy loss is incorporated by treating gluon radiation as an additional force term. The space-time evolution of the medium is modeled using a viscous hydrodynamic simulation. The hadronization of heavy quarks has a contribution based on the recombination mechanism. With respect to Ref. [45], the curves shown in the figure were obtained with a more recent parametrization for the nuclear shadowing of the parton distribution functions. This model provides a good description of the $R_{\rm AA}$ data in central collisions, but it yields a value of v_2 significantly smaller than the measured one (similarly to the WHDG and POWLANG models) and also underestimates the difference between the in-plane and the out-of-plane suppression.

Overall, the anisotropy is qualitatively described by the models that include both charm-quark energy loss in a geometrically anisotropic medium and mechanisms that transfer to charm quarks the elliptic flow induced during the system expansion. These mechanisms include collisional processes (MC@sHQ+EPOS, Coll+Rad(LPM) [74], BAMPS [21]) and resonance scattering with hadronization via recombination (TAMU elastic [43], UrQMD [44]) in a hydrodynamically expanding QGP. Models that do not include a collective expansion of the medium or lack a contribution to the hadronization of charm quarks from recombination with light quarks from the medium predict, in general, a smaller anisotropy than observed in the data. The comparison for $R_{\rm AA}$ and v_2 shows that it is challenging to simultaneously describe the large suppression of D mesons in central collisions and their anisotropy in noncentral collisions. In general, the models that are best in describing $R_{\rm AA}$ tend to underestimate v_2 and the models that describe v_2 tend to underestimate the measured $R_{\rm AA}$ at high $p_{\rm T}$. It is also worth noting that most of the calculations do reproduce the RHIC measurements of heavy-flavor decay electron $R_{\rm AA}$ and v_2.

VII. SUMMARY

We have presented a comprehensive set of results on the azimuthal anisotropy of charm production at central rapidity in Pb-Pb collisions at $\sqrt{s_{\rm NN}} = 2.76$ TeV, obtained by reconstructing the decays $D^0 \to K^-\pi^+$, $D^+ \to K^-\pi^+\pi^+$, and $D^{*+} \to D^0\pi^+$.

The azimuthal anisotropy parameter v_2 was measured with the EP, SP, and two-particle cumulant methods, as a function of transverse momentum for semicentral collisions in the 30%–50% quantile of the hadronic cross section. The measured anisotropy was found to be consistent among D-meson species, as well as for the three methods. The average v_2 of the three mesons in the interval $2 < p_{\rm T} < 6$ GeV/c is larger than zero with a significance of 5.7σ, combining statistical and systematic uncertainties. With a smaller significance, a positive v_2 is also observed for $p_{\rm T} > 6$ GeV/c, likely to originate from a path-length dependence of the partonic energy loss. The azimuthal anisotropy of D^0 mesons, which have larger statistical significance than D^+ and D^{*+}, was also measured in the centrality classes 0%–10% and 10%–30%. For all three centrality classes, the D^0 meson v_2 is comparable in magnitude to that of inclusive charged particles. An indication for a decrease of v_2 towards more central collisions was observed for $3 < p_{\rm T} < 6$ GeV/c.

The anisotropy was also quantified in terms of the D^0 meson nuclear modification factor $R_{\rm AA}$, measured in the direction of the EP and orthogonal to it. For $p_{\rm T} > 3$ GeV/c, a stronger suppression relative to proton-proton collisions is observed in the out-of-plane direction, where the average path length of heavy quarks through the medium is larger.

The results indicate that, during the collective expansion of the medium, the interactions between its constituents and charm quarks transfer to the latter information on the azimuthal anisotropy of the system.

The new results for v_2 and $R_{\rm AA}$ measured in and out of the EP, as well as previously published $R_{\rm AA}$ in the most central collisions [13], were compared with model calculations. The anisotropy is best described by the models that include mechanisms, like collisional energy loss, that transfer to charm quarks the elliptic flow induced during the system expansion. In some of these models the charmed meson v_2 is further enhanced by charm-quark recombination with light quarks from the medium. However, it is challenging for models to describe simultaneously the large suppression of D mesons in central collisions and their anisotropy in noncentral collisions. The results reported in this article provide important constraints on the mechanisms of heavy-quark energy loss and on the transport properties of the expanding medium produced in high-energy heavy-ion collisions.

ACKNOWLEDGMENTS

The ALICE Collaboration would like to thank all its engineers and technicians for their invaluable contributions to the construction of the experiment and the CERN accelerator teams for the outstanding performance of the LHC complex. The ALICE Collaboration gratefully acknowledges the resources and support provided by all Grid centers and the Worldwide LHC Computing Grid (WLCG) collaboration. The ALICE Collaboration would like to thank the authors of the theoretical calculations for providing their results. The ALICE Collaboration acknowledges the following funding agencies for their support in building and running the ALICE detector: State Committee of Science, World Federation of Scientists (WFS), and Swiss Fonds Kidagan, Armenia; Conselho Nacional de Desenvolvimento Científico e Tecnológico (CNPq), Financiadora de Estudos e Projetos (FINEP), Fundação de Amparo à Pesquisa do Estado de São Paulo (FAPESP); National Natural Science Foundation of China (NSFC), the

Chinese Ministry of Education (CMOE) and the Ministry of Science and Technology of China (MSTC); Ministry of Education and Youth of the Czech Republic; Danish Natural Science Research Council, the Carlsberg Foundation, and the Danish National Research Foundation; The European Research Council under the European Community's Seventh Framework Programme; Helsinki Institute of Physics and the Academy of Finland; French CNRS-IN2P3, the "Region Pays de Loire", "Region Alsace", "Region Auvergne", and CEA, France; German BMBF and the Helmholtz Association; General Secretariat for Research and Technology, Ministry of Development, Greece; Hungarian OTKA and National Office for Research and Technology (NKTH); Department of Atomic Energy and Department of Science and Technology of the Government of India; Istituto Nazionale di Fisica Nucleare (INFN) and Centro Fermi-Museo Storico della Fisica e Centro Studi e Ricerche "Enrico Fermi", Italy; MEXT Grant-in-Aid for Specially Promoted Research, Japan; Joint Institute for Nuclear Research, Dubna; National Research Foundation of Korea (NRF); CONACYT, DGAPA, México, ALFA-EC and the EPLANET Program (European Particle Physics Latin American Network); Stichting voor Fundamenteel Onderzoek der Materie (FOM) and the Nederlandse Organisatie voor Wetenschappelijk Onderzoek (NWO), Netherlands; Research Council of Norway (NFR); Polish Ministry of Science and Higher Education and National Science Centre, Poland; Ministry of National Education/Institute for Atomic Physics and CNCS-UEFISCDI, Romania; Ministry of Education and Science of Russian Federation, Russian Academy of Sciences, Russian Federal Agency of Atomic Energy, Russian Federal Agency for Science and Innovations, and The Russian Foundation for Basic Research; Ministry of Education of Slovakia; Department of Science and Technology, South Africa; CIEMAT, EELA, Ministerio de Economía y Competitividad (MINECO) of Spain, Xunta de Galicia (Consellería de Educación), CEADEN; Cubaenergía, Cuba; IAEA (International Atomic Energy Agency); Swedish Research Council (VR) and Knut & Alice Wallenberg Foundation (KAW); Ukraine Ministry of Education and Science; United Kingdom Science and Technology Facilities Council (STFC); The United States Department of Energy, the United States National Science Foundation, the State of Texas, and the State of Ohio.

[1] F. Karsch, J. Phys. Conf. Ser. **46**, 122 (2006).
[2] S. Borsanyi *et al.* (Wuppertal-Budapest Collaboration), J. High Energy Phys. 09 (2010) 073; 11 (2010) 077.
[3] A. Bazavov *et al.*, Phys. Rev. D **85**, 054503 (2012).
[4] P. Petreczky, PoS (**Confinement X**), 028 (2012).
[5] P. Braun-Munzinger, J. Phys. G **34**, S471 (2007).
[6] M. Gyulassy and M. Plumer, Phys. Lett. B **243**, 432 (1990).
[7] R. Baier, Y. L. Dokshitzer, A. H. Mueller, S. Peigne, and D. Schiff, Nucl. Phys. B **484**, 265 (1997).
[8] M. H. Thoma and M. Gyulassy, Nucl. Phys. B **351**, 491 (1991); E. Braaten and M. H. Thoma, Phys. Rev. D **44**, 1298 (1991); **44**, R2625 (1991).
[9] R. J. Glauber, in *Lectures in Theoretical Physics* (Interscience, New York, 1959), Vol. 1, p. 315; M. Miller *et al.*, Annu. Rev. Nucl. Part. Sci. **57**, 205 (2007).
[10] S. S. Adler *et al.* (PHENIX Collaboration), Phys. Rev. Lett. **96**, 032301 (2006); A. Adare *et al.* (PHENIX Collaboration), Phys. Rev. C **84**, 044905 (2011).
[11] B. I. Abelev *et al.* (STAR Collaboration), Phys. Rev. Lett. **98**, 192301 (2007); **106**, 159902(E) (2011).
[12] L. Adamczyk *et al.* (STAR Collaboration), arXiv:1404.6185 [nucl-ex].
[13] B. Abelev *et al.* (ALICE Collaboration), J. High Energy Phys. 09 (2012) 112.
[14] B. Abelev *et al.* (ALICE Collaboration), Phys. Rev. Lett. **109**, 112301 (2012).
[15] S. Chatrchyan *et al.* (CMS Collaboration), J. High Energy Phys. 05 (2012) 063.
[16] N. Armesto, A. Dainese, C. A. Salgado, and U. A. Wiedemann, Phys. Rev. D **71**, 054027 (2005).
[17] Y. He, I. Vitev, and B.-W. Zhang, Phys. Lett. B **713**, 224 (2012).
[18] S. Wicks, W. A. Horowitz, M. Djordjevic, and M. Gyulassy, Nucl. Phys. A **784**, 426 (2007); W. A. Horowitz and M. Gyulassy, *ibid.* **872**, 265 (2011); W. A. Horowitz, AIP Conf. Proc. **1441**, 889 (2012).
[19] W. M. Alberico *et al.*, Eur. Phys. J. C **71**, 1666 (2011); J. Phys. G **38**, 124144 (2011).
[20] P. B. Gossiaux, R. Bierkandt, and J. Aichelin, Phys. Rev. C **79**, 044906 (2009); P. B. Gossiaux, J. Aichelin, T. Gousset, and V. Guiho, J. Phys. G **37**, 094019 (2010).
[21] J. Uphoff, O. Fochler, Z. Xu, and C. Greiner, Phys. Rev. C **84**, 024908 (2011); O. Fochler, J. Uphoff, Z. Xu, and C. Greiner, J. Phys. G **38**, 124152 (2011); Phys. Lett. B **717**, 430 (2012).
[22] A. Buzzatti and M. Gyulassy, Phys. Rev. Lett. **108**, 022301 (2012).
[23] S. Batsouli, S. Kelly, M. Gyulassy, and J. L. Nagle, Phys. Lett. B **557**, 26 (2003).
[24] V. Greco, C. M. Ko, and R. Rapp, Phys. Lett. B **595**, 202 (2004).
[25] A. Andronic, P. Braun-Munzinger, K. Redlich, and J. Stachel, Phys. Lett. B **571**, 36 (2003).
[26] M. Gyulassy, I. Vitev, and X. N. Wang, Phys. Rev. Lett. **86**, 2537 (2001).
[27] E. V. Shuryak, Phys. Rev. C **66**, 027902 (2002).
[28] J. Y. Ollitrault, Phys. Rev. D **46**, 229 (1992).
[29] P. F. Kolb and U. W. Heinz, in *Quark Gluon Plasma 3*, edited by R. C. Hwa *et al.* (World Scientific, Singapore, 2004), pp. 634–714.
[30] J. Adams *et al.* (STAR Collaboration), Phys. Rev. C **72**, 014904 (2005).
[31] S. Afanasiev *et al.* (PHENIX Collaboration), Phys. Rev. C **80**, 054907 (2009).
[32] K. Aamodt *et al.* (ALICE Collaboration), Phys. Rev. Lett. **105**, 252302 (2010).

[33] B. Abelev *et al.* (ALICE Collaboration), Phys. Lett. B **719**, 18 (2013).
[34] G. Aad *et al.* (ATLAS Collaboration), Phys. Rev. C **86**, 014907 (2012).
[35] S. Chatrchyan *et al.* (CMS Collaboration), Phys. Rev. C **87**, 014902 (2013).
[36] M. Luzum and P. Romatschke, Phys. Rev. Lett. **103**, 262302 (2009).
[37] E. Abbas *et al.* (ALICE Collaboration), Phys. Rev. Lett. **111**, 162301 (2013).
[38] Y. Liu, N. Xu, and P. Zhuang, Nucl. Phys. A **834**, 317c (2010).
[39] X. Zhao, A. Emerick, and R. Rapp, Nucl. Phys. A **904-905**, 611c (2013).
[40] G. D. Moore and D. Teaney, Phys. Rev. C **71**, 064904 (2005).
[41] H. van Hees, V. Greco, and R. Rapp, Phys. Rev. C **73**, 034913 (2006); H. van Hees, M. Mannarelli, V. Greco, and R. Rapp, Phys. Rev. Lett. **100**, 192301 (2008).
[42] M. He, R. J. Fries, and R. Rapp, Phys. Rev. C **86**, 014903 (2012).
[43] M. He, R. J. Fries, and R. Rapp, arXiv:1401.3817 [nucl-th].
[44] T. Lang, H. van Hees, J. Steinheimer, and M. Bleicher, arXiv:1211.6912 [hep-ph]; T. Lang, H. van Hees, J. Steinheimer, Y.-P. Yan, and M. Bleicher, J. Phys. Conf. Ser. **426**, 012032 (2013).
[45] S. Cao, G.-Y. Qin, and S. A. Bass, Phys. Rev. C **88**, 044907 (2013).
[46] B. Abelev *et al.* (ALICE Collaboration), Phys. Rev. Lett. **111**, 102301 (2013).
[47] K. Aamodt *et al.* (ALICE Collaboration), J. Instrum. **3**, S08002 (2008).
[48] K. Aamodt *et al.* (ALICE Collaboration), J. Instrum. **5**, P03003 (2010).
[49] A. Rossi (for the ALICE Collaboration), PoS (**VERTEX 2010**), 017 (2010).
[50] J. Alme *et al.*, Nucl. Instrum. Methods A **622**, 316 (2010).
[51] A. Akindinov *et al.*, Eur. Phys. J. Plus **128**, 44 (2013).
[52] E. Abbas *et al.* (ALICE Collaboration), J. Instrum. **8**, P10016 (2013).
[53] B. Abelev *et al.* (ALICE Collaboration), Phys. Rev. C **88**, 044909 (2013).
[54] J. Beringer *et al.* (Particle Data Group), Phys. Rev. D **86**, 010001 (2012).
[55] B. Abelev *et al.* (ALICE Collaboration), J. High Energy Phys. 01 (2012) 128.
[56] B. Abelev *et al.* (ALICE Collaboration), J. High Energy Phys. 07 (2012) 191.
[57] A. M. Poskanzer and S. A. Voloshin, Phys. Rev. C **58**, 1671 (1998).
[58] C. Adler *et al.* (STAR Collaboration), Phys. Rev. C **66**, 034904 (2002).
[59] A. Bilandzic, R. Snellings, and S. Voloshin, Phys. Rev. C **83**, 044913 (2011).
[60] I. Selyuzhenkov and S. Voloshin, Phys. Rev. C **77**, 034904 (2008).
[61] M. Luzum and J.-Y. Ollitrault, Phys. Rev. C **87**, 044907 (2013).
[62] K. Aamodt *et al.* (ALICE Collaboration), Phys. Lett. B **708**, 249 (2012).
[63] K. Aamodt *et al.* (ALICE Collaboration), Phys. Rev. Lett. **107**, 032301 (2011).
[64] R. Brun *et al.*, CERN Program Library Long Write-up, W5013, GEANT Detector Description and Simulation Tool (1994).
[65] X.-N. Wang and M. Gyulassy, Phys. Rev. D **44**, 3501 (1991).
[66] T. Sjöstrand, S. Mrenna, and P. Skands, J. High Energy Phys. 05 (2006) 026.
[67] P. Z. Skands, arXiv:0905.3418 [hep-ph].
[68] M. Cacciari, S. Frixione, N. Houdeau, M. L. Mangano, P. Nason, and G. Ridolfi, J. High Energy Phys. 10 (2012) 137.
[69] D. J. Lange, Nucl. Instrum. Methods A **462**, 152 (2001).
[70] A. Grelli (for the ALICE Collaboration), arXiv:1310.7366 [hep-ex].
[71] CMS Collaboration, CMS-PAS-HIN-12-014 (2012).
[72] R. Averbeck, N. Bastid, Z. C. del Valle, P. Crochet, A. Dainese, and X. Zhang, arXiv:1107.3243 [hep-ph].
[73] M. Djordjevic and M. Gyulassy, Nucl. Phys. A **733**, 265 (2004).
[74] M. Nahrgang, J. Aichelin, P. B. Gossiaux, and K. Werner, Phys. Rev. C **89**, 014905 (2014).
[75] R. Baier, D. Schiff, and B. G. Zakharov, Annu. Rev. Nucl. Part. Sci. **50**, 37 (2000).
[76] K. Werner, I. Karpenko, T. Pierog, M. Bleicher, and K. Mikhailov, Phys. Rev. C **82**, 044904 (2010); K. Werner, I. K arpenko, M. Bleicher, T. Pierog, and S. Porteboeuf-Houssais, *ibid.* **85**, 064907 (2012).
[77] S. A. Bass *et al.*, Prog. Part. Nucl. Phys. **41**, 255 (1998); M. Bleicher *et al.*, J. Phys. G **25**, 1859 (1999).

B. Abelev,[1] J. Adam,[2] D. Adamová,[3] M. M. Aggarwal,[4] M. Agnello,[5,6] A. Agostinelli,[7] N. Agrawal,[8] Z. Ahammed,[9] N. Ahmad,[10] I. Ahmed,[11] S. U. Ahn,[12] S. A. Ahn,[12] I. Aimo,[5,6] S. Aiola,[13] M. Ajaz,[11] A. Akindinov,[14] S. N. Alam,[9] D. Aleksandrov,[15] B. Alessandro,[5] D. Alexandre,[16] A. Alici,[17,18] A. Alkin,[19] J. Alme,[20] T. Alt,[21] S. Altinpinar,[22] I. Altsybeev,[23] C. Alves Garcia Prado,[24] C. Andrei,[25] A. Andronic,[26] V. Anguelov,[27] J. Anielski,[28] T. Antičić,[29] F. Antinori,[30] P. Antonioli,[18] L. Aphecetche,[31] H. Appelshäuser,[32] S. Arcelli,[7] N. Armesto,[33] R. Arnaldi,[5] T. Aronsson,[13] I. C. Arsene,[26] M. Arslandok,[32] A. Augustinus,[34] R. Averbeck,[26] T. C. Awes,[35] M. D. Azmi,[36] M. Bach,[21] A. Badalà,[37] Y. W. Baek,[38,39] S. Bagnasco,[5] R. Bailhache,[32] R. Bala,[40] A. Baldisseri,[41] F. Baltasar Dos Santos Pedrosa,[34] R. C. Baral,[42] R. Barbera,[43] F. Barile,[44] G. G. Barnaföldi,[45] L. S. Barnby,[16] V. Barret,[38] J. Bartke,[46] M. Basile,[7] N. Bastid,[38] S. Basu,[9] B. Bathen,[28] G. Batigne,[31] A. Batista Camejo,[38] B. Batyunya,[47] P. C. Batzing,[48] C. Baumann,[32] I. G. Bearden,[49] H. Beck,[32] C. Bedda,[6] N. K. Behera,[8] I. Belikov,[50] F. Bellini,[7] R. Bellwied,[51] E. Belmont-Moreno,[52] R. Belmont III,[53] V. Belyaev,[54] G. Bencedi,[45] S. Beole,[55] I. Berceanu,[25] A. Bercuci,[25] Y. Berdnikov,[56,57] D. Berenyi,[45] M. E. Berger,[58] R. A. Bertens,[59] D. Berzano,[55] L. Betev,[34] A. Bhasin,[40] I. R. Bhat,[40] A. K. Bhati,[4] B. Bhattacharjee,[60] J. Bhom,[61] L. Bianchi,[55] N. Bianchi,[62] C. Bianchin,[59] J. Bielčík,[2] J. Bielčíková,[3] A. Bilandzic,[49] S. Bjelogrlic,[59] F. Blanco,[63] D. Blau,[15] C. Blume,[32] F. Bock,[27,64] A. Bogdanov,[54] H. Bøggild,[49] M. Bogolyubsky,[65] F. V. Böhmer,[58] L. Boldizsár,[45] M. Bombara,[66] J. Book,[32] H. Borel,[41] A. Borissov,[67,53] F. Bossú,[68]

M. Botje,[69] E. Botta,[55] S. Böttger,[70] P. Braun-Munzinger,[26] M. Bregant,[24] T. Breitner,[70] T. A. Broker,[32] T. A. Browning,[71] M. Broz,[2] E. Bruna,[5] G. E. Bruno,[44] D. Budnikov,[72] H. Buesching,[32] S. Bufalino,[5] P. Buncic,[34] O. Busch,[27] Z. Buthelezi,[68] D. Caffarri,[73] X. Cai,[74] H. Caines,[13] L. Calero Diaz,[62] A. Caliva,[59] E. Calvo Villar,[75] P. Camerini,[76] F. Carena,[34] W. Carena,[34] J. Castillo Castellanos,[41] E. A. R. Casula,[77] V. Catanescu,[25] C. Cavicchioli,[34] C. Ceballos Sanchez,[78] J. Cepila,[2] P. Cerello,[5] B. Chang,[79] S. Chapeland,[34] J. L. Charvet,[41] S. Chattopadhyay,[9] S. Chattopadhyay,[80] V. Chelnokov,[19] M. Cherney,[81] C. Cheshkov,[82] B. Cheynis,[82] V. Chibante Barroso,[34] D. D. Chinellato,[51] P. Chochula,[34] M. Chojnacki,[49] S. Choudhury,[9] P. Christakoglou,[69] C. H. Christensen,[49] P. Christiansen,[83] T. Chujo,[61] S. U. Chung,[67] C. Cicalo,[84] L. Cifarelli,[7,17] F. Cindolo,[18] J. Cleymans,[36] F. Colamaria,[44] D. Colella,[44] A. Collu,[77] M. Colocci,[7] G. Conesa Balbastre,[85] Z. Conesa del Valle,[86] M. E. Connors,[13] J. G. Contreras,[87] T. M. Cormier,[53] Y. Corrales Morales,[55] P. Cortese,[88] I. Cortés Maldonado,[89] M. R. Cosentino,[24] F. Costa,[34] P. Crochet,[38] R. Cruz Albino,[87] E. Cuautle,[90] L. Cunqueiro,[62] A. Dainese,[30] R. Dang,[74] A. Danu,[91] D. Das,[80] I. Das,[86] K. Das,[80] S. Das,[92] A. Dash,[93] S. Dash,[8] S. De,[9] H. Delagrange,[31,*] A. Deloff,[94] E. Dénes,[45] G. D'Erasmo,[44] A. De Caro,[95,17] G. de Cataldo,[96] J. de Cuveland,[21] A. De Falco,[77] D. De Gruttola,[95,17] N. De Marco,[5] S. De Pasquale,[95] R. de Rooij,[59] M. A. Diaz Corchero,[63] T. Dietel,[28] P. Dillenseger,[32] R. Divià,[34] D. Di Bari,[44] S. Di Liberto,[97] A. Di Mauro,[34] P. Di Nezza,[62] Ø. Djuvsland,[22] A. Dobrin,[59] T. Dobrowolski,[94] D. Domenicis Gimenez,[24] B. Dönigus,[32] O. Dordic,[48] S. Dørheim,[58] A. K. Dubey,[9] A. Dubla,[59] L. Ducroux,[82] P. Dupieux,[38] A. K. Dutta Majumdar,[80] T. E. Hilden,[98] R. J. Ehlers,[13] D. Elia,[96] H. Engel,[70] B. Erazmus,[34,31] H. A. Erdal,[20] D. Eschweiler,[21] B. Espagnon,[86] M. Esposito,[34] M. Estienne,[31] S. Esumi,[61] D. Evans,[16] S. Evdokimov,[65] D. Fabris,[30] J. Faivre,[85] D. Falchieri,[7] A. Fantoni,[62] M. Fasel,[27] D. Fehlker,[22] L. Feldkamp,[28] D. Felea,[91] A. Feliciello,[5] G. Feofilov,[23] J. Ferencei,[3] A. Fernández Téllez,[89] E. G. Ferreiro,[33] A. Ferretti,[55] A. Festanti,[73] J. Figiel,[46] M. A. S. Figueredo,[99] S. Filchagin,[72] D. Finogeev,[100] F. M. Fionda,[44] E. M. Fiore,[44] E. Floratos,[101] M. Floris,[34] S. Foertsch,[68] P. Foka,[26] S. Fokin,[15] E. Fragiacomo,[102] A. Francescon,[34,73] U. Frankenfeld,[26] U. Fuchs,[34] C. Furget,[85] M. Fusco Girard,[95] J. J. Gaardhøje,[49] M. Gagliardi,[55] A. M. Gago,[75] M. Gallio,[55] D. R. Gangadharan,[103] P. Ganoti,[35] C. Garabatos,[26] E. Garcia-Solis,[104] C. Gargiulo,[34] I. Garishvili,[1] J. Gerhard,[21] M. Germain,[31] A. Gheata,[34] M. Gheata,[34,91] B. Ghidini,[44] P. Ghosh,[9] S. K. Ghosh,[92] P. Gianotti,[62] P. Giubellino,[34] E. Gladysz-Dziadus,[46] P. Glässel,[27] A. Gomez Ramirez,[70] P. González-Zamora,[63] S. Gorbunov,[21] L. Görlich,[46] S. Gotovac,[105] L. K. Graczykowski,[106] R. Grajcarek,[27] A. Grelli,[59] A. Grigoras,[34] C. Grigoras,[34] V. Grigoriev,[54] A. Grigoryan,[107] S. Grigoryan,[47] B. Grinyov,[19] N. Grion,[102] J. F. Grosse-Oetringhaus,[34] J.-Y. Grossiord,[82] R. Grosso,[34] F. Guber,[100] R. Guernane,[85] B. Guerzoni,[7] M. Guilbaud,[82] K. Gulbrandsen,[49] H. Gulkanyan,[107] M. Gumbo,[36] T. Gunji,[108] A. Gupta,[40] R. Gupta,[40] K. H. Khan,[11] R. Haake,[28] Ø. Haaland,[22] C. Hadjidakis,[86] M. Haiduc,[91] H. Hamagaki,[108] G. Hamar,[45] L. D. Hanratty,[16] A. Hansen,[49] J. W. Harris,[13] H. Hartmann,[21] A. Harton,[104] D. Hatzifotiadou,[18] S. Hayashi,[108] S. T. Heckel,[32] M. Heide,[28] H. Helstrup,[20] A. Herghelegiu,[25] G. Herrera Corral,[87] B. A. Hess,[109] K. F. Hetland,[20] B. Hippolyte,[50] J. Hladky,[110] P. Hristov,[34] M. Huang,[22] T. J. Humanic,[103] N. Hussain,[60] D. Hutter,[21] D. S. Hwang,[111] R. Ilkaev,[72] I. Ilkiv,[94] M. Inaba,[61] G. M. Innocenti,[55] C. Ionita,[34] M. Ippolitov,[15] M. Irfan,[10] M. Ivanov,[26] V. Ivanov,[57] A. Jachołkowski,[43] P. M. Jacobs,[64] C. Jahnke,[24] H. J. Jang,[12] M. A. Janik,[106] P. H. S. Y. Jayarathna,[51] C. Jena,[73] S. Jena,[51] R. T. Jimenez Bustamante,[90] P. G. Jones,[16] H. Jung,[39] A. Jusko,[16] V. Kadyshevskiy,[47] S. Kalcher,[21] P. Kalinak,[112] A. Kalweit,[34] J. Kamin,[32] J. H. Kang,[113] V. Kaplin,[54] S. Kar,[9] A. Karasu Uysal,[114] O. Karavichev,[100] T. Karavicheva,[100] E. Karpechev,[100] U. Kebschull,[70] R. Keidel,[115] D. L. D. Keijdener,[59] M. M. Khan,[116,10] P. Khan,[80] S. A. Khan,[9] A. Khanzadeev,[57] Y. Kharlov,[65] B. Kileng,[20] B. Kim,[113] D. W. Kim,[12,39] D. J. Kim,[79] J. S. Kim,[39] M. Kim,[39] M. Kim,[113] S. Kim,[111] T. Kim,[113] S. Kirsch,[21] I. Kisel,[21] S. Kiselev,[14] A. Kisiel,[106] G. Kiss,[45] J. L. Klay,[117] J. Klein,[27] C. Klein-Bösing,[28] A. Kluge,[34] M. L. Knichel,[26] A. G. Knospe,[118] C. Kobdaj,[34,119] M. Kofarago,[34] M. K. Köhler,[26] T. Kollegger,[21] A. Kolojvari,[23] V. Kondratiev,[23] N. Kondratyeva,[54] A. Konevskikh,[100] V. Kovalenko,[23] M. Kowalski,[46] S. Kox,[85] G. Koyithatta Meethaleveedu,[8] J. Kral,[79] I. Králik,[112] F. Kramer,[32] A. Kravčáková,[66] M. Krelina,[2] M. Kretz,[21] M. Krivda,[16,112] F. Krizek,[3] E. Kryshen,[34] M. Krzewicki,[26] V. Kučera,[3] Y. Kucheriaev,[15,*] T. Kugathasan,[34] C. Kuhn,[50] P. G. Kuijer,[69] I. Kulakov,[32] J. Kumar,[8] P. Kurashvili,[94] A. Kurepin,[100] A. B. Kurepin,[100] A. Kuryakin,[72] S. Kushpil,[3] M. J. Kweon,[27] Y. Kwon,[113] P. Ladron de Guevara,[90] C. Lagana Fernandes,[24] I. Lakomov,[86] R. Langoy,[120] C. Lara,[70] A. Lardeux,[31] A. Lattuca,[55] S. L. La Pointe,[59] P. La Rocca,[43] R. Lea,[76] L. Leardini,[27] G. R. Lee,[16] I. Legrand,[34] J. Lehnert,[32] R. C. Lemmon,[121] V. Lenti,[96] E. Leogrande,[59] M. Leoncino,[55] I. León Monzón,[122] P. Lévai,[45] S. Li,[38,74] J. Lien,[120] R. Lietava,[16] S. Lindal,[48] V. Lindenstruth,[21] C. Lippmann,[26] M. A. Lisa,[103] H. M. Ljunggren,[83] D. F. Lodato,[59] P. I. Loenne,[22] V. R. Loggins,[53] V. Loginov,[54] D. Lohner,[27] C. Loizides,[64] X. Lopez,[38] E. López Torres,[78] X.-G. Lu,[27] P. Luettig,[32] M. Lunardon,[73] G. Luparello,[59] R. Ma,[13] A. Maevskaya,[100] M. Mager,[34] D. P. Mahapatra,[42] S. M. Mahmood,[48] A. Maire,[27] R. D. Majka,[13] M. Malaev,[57] I. Maldonado Cervantes,[90] L. Malinina,[123,47] D. Mal'Kevich,[14] P. Malzacher,[26] A. Mamonov,[72] L. Manceau,[5] V. Manko,[15] F. Manso,[38] V. Manzari,[96] M. Marchisone,[38,55] J. Mareš,[110] G. V. Margagliotti,[76] A. Margotti,[18] A. Marín,[26] C. Markert,[118] M. Marquard,[32] I. Martashvili,[124] N. A. Martin,[26] P. Martinengo,[34] M. I. Martínez,[89] G. Martínez García,[31] J. Martin Blanco,[31] Y. Martynov,[19] A. Mas,[31] S. Masciocchi,[26] M. Masera,[55] A. Masoni,[84] L. Massacrier,[31] A. Mastroserio,[44] A. Matyja,[46] C. Mayer,[46] J. Mazer,[124] M. A. Mazzoni,[97] F. Meddi,[125] A. Menchaca-Rocha,[52] J. Mercado Pérez,[27] M. Meres,[126] Y. Miake,[61] K. Mikhaylov,[47,14] L. Milano,[34] J. Milosevic,[127,48] A. Mischke,[59] A. N. Mishra,[128] D. Miśkowiec,[26] J. Mitra,[9] C. M. Mitu,[91] J. Mlynarz,[53] N. Mohammadi,[59] B. Mohanty,[129,9] L. Molnar,[50] L. Montaño Zetina,[87] E. Montes,[63] M. Morando,[73] D. A. Moreira De Godoy,[24] S. Moretto,[73] A. Morsch,[34] V. Muccifora,[62] E. Mudnic,[105] D. Mühlheim,[28] S. Muhuri,[9] M. Mukherjee,[9] H. Müller,[34] M. G. Munhoz,[24] S. Murray,[36] L. Musa,[34] J. Musinsky,[112] B. K. Nandi,[8] R. Nania,[18] E. Nappi,[96] C. Nattrass,[124] K. Nayak,[129] T. K. Nayak,[9]

S. Nazarenko,[72] A. Nedosekin,[14] M. Nicassio,[26] M. Niculescu,[34,91] B. S. Nielsen,[49] S. Nikolaev,[15] S. Nikulin,[15] V. Nikulin,[57] B. S. Nilsen,[81] F. Noferini,[17,18] P. Nomokonov,[47] G. Nooren,[59] J. Norman,[99] A. Nyanin,[15] J. Nystrand,[22] H. Oeschler,[27] S. Oh,[13] S. K. Oh,[39,†] A. Okatan,[114] L. Olah,[45] J. Oleniacz,[106] A. C. Oliveira Da Silva,[24] J. Onderwaater,[26] C. Oppedisano,[5] A. Ortiz Velasquez,[83] G. Ortona,[55] A. Oskarsson,[83] J. Otwinowski,[26] K. Oyama,[27] P. Sahoo,[128] Y. Pachmayer,[27] M. Pachr,[2] P. Pagano,[95] G. Paić,[90] F. Painke,[21] C. Pajares,[33] S. K. Pal,[9] A. Palmeri,[37] D. Pant,[8] V. Papikyan,[107] G. S. Pappalardo,[37] P. Pareek,[128] W. J. Park,[26] S. Parmar,[4] A. Passfeld,[28] D. I. Patalakha,[65] V. Paticchio,[96] B. Paul,[80] T. Pawlak,[106] T. Peitzmann,[59] H. Pereira Da Costa,[41] E. Pereira De Oliveira Filho,[24] D. Peresunko,[15] C. E. Pérez Lara,[69] A. Pesci,[18] V. Peskov,[32] Y. Pestov,[130] V. Petráček,[2] M. Petran,[2] M. Petris,[25] M. Petrovici,[25] C. Petta,[43] S. Piano,[102] M. Pikna,[126] P. Pillot,[31] O. Pinazza,[18,34] L. Pinsky,[51] D. B. Piyarathna,[51] M. Płoskoń,[64] M. Planinic,[131,29] J. Pluta,[106] S. Pochybova,[45] P. L. M. Podesta-Lerma,[122] M. G. Poghosyan,[34] E. H. O. Pohjoisaho,[98] B. Polichtchouk,[65] N. Poljak,[29] A. Pop,[25] S. Porteboeuf-Houssais,[38] J. Porter,[64] B. Potukuchi,[40] S. K. Prasad,[53] R. Preghenella,[18,17] F. Prino,[5] C. A. Pruneau,[53] I. Pshenichnov,[100] G. Puddu,[77] P. Pujahari,[53] V. Punin,[72] J. Putschke,[53] H. Qvigstad,[48] A. Rachevski,[102] S. Raha,[92] J. Rak,[79] A. Rakotozafindrabe,[41] L. Ramello,[88] R. Raniwala,[132] S. Raniwala,[132] S. S. Räsänen,[98] B. T. Rascanu,[32] D. Rathee,[4] A. W. Rauf,[11] V. Razazi,[77] K. F. Read,[124] J. S. Real,[85] K. Redlich,[133,94] R. J. Reed,[13] A. Rehman,[22] P. Reichelt,[32] M. Reicher,[59] F. Reidt,[34] R. Renfordt,[32] A. R. Reolon,[62] A. Reshetin,[100] F. Rettig,[21] J.-P. Revol,[34] K. Reygers,[27] V. Riabov,[57] R. A. Ricci,[134] T. Richert,[83] M. Richter,[48] P. Riedler,[34] W. Riegler,[34] F. Riggi,[43] A. Rivetti,[5] E. Rocco,[59] M. Rodríguez Cahuantzi,[89] A. Rodriguez Manso,[69] K. Røed,[48] E. Rogochaya,[47] S. Rohni,[40] D. Rohr,[21] D. Röhrich,[22] R. Romita,[121] F. Ronchetti,[62] L. Ronflette,[31] P. Rosnet,[38] A. Rossi,[34] F. Roukoutakis,[101] A. Roy,[128] C. Roy,[50] P. Roy,[80] A. J. Rubio Montero,[63] R. Rui,[76] R. Russo,[55] E. Ryabinkin,[15] Y. Ryabov,[57] A. Rybicki,[46] S. Sadovsky,[65] K. Šafařík,[34] B. Sahlmuller,[32] R. Sahoo,[128] P. K. Sahu,[42] J. Saini,[9] S. Sakai,[64] C. A. Salgado,[33] J. Salzwedel,[103] S. Sambyal,[40] V. Samsonov,[57] X. Sanchez Castro,[50] F. J. Sánchez Rodríguez,[122] L. Šándor,[112] A. Sandoval,[52] M. Sano,[61] G. Santagati,[43] D. Sarkar,[9] E. Scapparone,[18] F. Scarlassara,[73] R. P. Scharenberg,[71] C. Schiaua,[25] R. Schicker,[27] C. Schmidt,[26] H. R. Schmidt,[109] S. Schuchmann,[32] J. Schukraft,[34] M. Schulc,[2] T. Schuster,[13] Y. Schutz,[31,34] K. Schwarz,[26] K. Schweda,[26] G. Scioli,[7] E. Scomparin,[5] R. Scott,[124] G. Segato,[73] J. E. Seger,[81] Y. Sekiguchi,[108] I. Selyuzhenkov,[26] J. Seo,[67] E. Serradilla,[63,52] A. Sevcenco,[91] A. Shabetai,[31] G. Shabratova,[47] R. Shahoyan,[34] A. Shangaraev,[65] N. Sharma,[124] S. Sharma,[40] K. Shigaki,[135] K. Shtejer,[55] Y. Sibiriak,[15] E. Sicking,[28,34] S. Siddhanta,[84] T. Siemiarczuk,[94] D. Silvermyr,[35] C. Silvestre,[85] G. Simatovic,[131] R. Singaraju,[9] R. Singh,[40] S. Singha,[9,129] V. Singhal,[9] B. C. Sinha,[9] T. Sinha,[80] B. Sitar,[126] M. Sitta,[88] T. B. Skaali,[48] K. Skjerdal,[22] M. Slupecki,[79] N. Smirnov,[13] R. J. M. Snellings,[59] C. Søgaard,[83] R. Soltz,[1] J. Song,[67] M. Song,[113] F. Soramel,[73] S. Sorensen,[124] M. Spacek,[2] E. Spiriti,[62] I. Sputowska,[46] M. Spyropoulou-Stassinaki,[101] B. K. Srivastava,[71] J. Stachel,[27] I. Stan,[91] G. Stefanek,[94] M. Steinpreis,[103] E. Stenlund,[83] G. Steyn,[68] J. H. Stiller,[27] D. Stocco,[31] M. Stolpovskiy,[65] P. Strmen,[126] A. A. P. Suaide,[24] T. Sugitate,[135] C. Suire,[86] M. Suleymanov,[11] R. Sultanov,[14] M. Šumbera,[3] T. Susa,[29] T. J. M. Symons,[64] A. Szabo,[126] A. Szanto de Toledo,[24] I. Szarka,[126] A. Szczepankiewicz,[34] M. Szymanski,[106] J. Takahashi,[93] M. A. Tangaro,[44] J. D. Tapia Takaki,[136,86] A. Tarantola Peloni,[32] A. Tarazona Martinez,[34] M. G. Tarzila,[25] A. Tauro,[34] G. Tejeda Muñoz,[89] A. Telesca,[34] C. Terrevoli,[77] J. Thäder,[26] D. Thomas,[59] R. Tieulent,[82] A. R. Timmins,[51] A. Toia,[30] V. Trubnikov,[19] W. H. Trzaska,[79] T. Tsuji,[108] A. Tumkin,[72] R. Turrisi,[30] T. S. Tveter,[48] K. Ullaland,[22] A. Uras,[82] G. L. Usai,[77] M. Vajzer,[3] M. Vala,[112,47] L. Valencia Palomo,[38] S. Vallero,[27] P. Vande Vyvre,[34] J. Van Der Maarel,[59] J. W. Van Hoorne,[34] M. van Leeuwen,[59] A. Vargas,[89] M. Vargyas,[79] R. Varma,[8] M. Vasileiou,[101] A. Vasiliev,[15] V. Vechernin,[23] M. Veldhoen,[59] A. Velure,[22] M. Venaruzzo,[76,134] E. Vercellin,[55] S. Vergara Limón,[89] R. Vernet,[137] M. Verweij,[53] L. Vickovic,[105] G. Viesti,[73] J. Viinikainen,[79] Z. Vilakazi,[68] O. Villalobos Baillie,[16] A. Vinogradov,[15] L. Vinogradov,[23] Y. Vinogradov,[72] T. Virgili,[95] Y. P. Viyogi,[9] A. Vodopyanov,[47] M. A. Völkl,[27] K. Voloshin,[14] S. A. Voloshin,[53] G. Volpe,[34] B. von Haller,[34] I. Vorobyev,[23] D. Vranic,[34,26] J. Vrláková,[66] B. Vulpescu,[38] A. Vyushin,[72] B. Wagner,[22] J. Wagner,[26] V. Wagner,[2] M. Wang,[74,31] Y. Wang,[27] D. Watanabe,[61] M. Weber,[51] J. P. Wessels,[28] U. Westerhoff,[28] J. Wiechula,[109] J. Wikne,[48] M. Wilde,[28] G. Wilk,[94] J. Wilkinson,[27] M. C. S. Williams,[18] B. Windelband,[27] M. Winn,[27] C. G. Yaldo,[53] Y. Yamaguchi,[108] H. Yang,[59] P. Yang,[74] S. Yang,[22] S. Yano,[135] S. Yasnopolskiy,[15] J. Yi,[67] Z. Yin,[74] I.-K. Yoo,[67] I. Yushmanov,[15] V. Zaccolo,[49] C. Zach,[2] A. Zaman,[11] C. Zampolli,[18] S. Zaporozhets,[47] A. Zarochentsev,[23] P. Závada,[110] N. Zaviyalov,[72] H. Zbroszczyk,[106] I. S. Zgura,[91] M. Zhalov,[57] H. Zhang,[74] X. Zhang,[74,64] Y. Zhang,[74] C. Zhao,[48] N. Zhigareva,[14] D. Zhou,[74] F. Zhou,[74] Y. Zhou,[59] Zhuo Zhou,[22] H. Zhu,[74] J. Zhu,[74] X. Zhu,[74] A. Zichichi,[17,7] A. Zimmermann,[27] M. B. Zimmermann,[28,34] G. Zinovjev,[19] Y. Zoccarato,[82] and M. Zyzak[32]

(ALICE Collaboration)

[1]*Lawrence Livermore National Laboratory, Livermore, California, USA*
[2]*Faculty of Nuclear Sciences and Physical Engineering, Czech Technical University in Prague, Prague, Czech Republic*
[3]*Nuclear Physics Institute, Academy of Sciences of the Czech Republic, Řež u Prahy, Czech Republic*
[4]*Physics Department, Panjab University, Chandigarh, India*
[5]*Sezione INFN, Turin, Italy*
[6]*Politecnico di Torino, Turin, Italy*
[7]*Dipartimento di Fisica e Astronomia dell'Università and Sezione INFN, Bologna, Italy*
[8]*Indian Institute of Technology Bombay (IIT), Mumbai, India*
[9]*Variable Energy Cyclotron Centre, Kolkata, India*

[10]*Department of Physics, Aligarh Muslim University, Aligarh, India*
[11]*COMSATS Institute of Information Technology (CIIT), Islamabad, Pakistan*
[12]*Korea Institute of Science and Technology Information, Daejeon, South Korea*
[13]*Yale University, New Haven, Connecticut, USA*
[14]*Institute for Theoretical and Experimental Physics, Moscow, Russia*
[15]*Russian Research Centre Kurchatov Institute, Moscow, Russia*
[16]*School of Physics and Astronomy, University of Birmingham, Birmingham, United Kingdom*
[17]*Centro Fermi-Museo Storico della Fisica e Centro Studi e Ricerche "Enrico Fermi," Rome, Italy*
[18]*Sezione INFN, Bologna, Italy*
[19]*Bogolyubov Institute for Theoretical Physics, Kiev, Ukraine*
[20]*Faculty of Engineering, Bergen University College, Bergen, Norway*
[21]*Frankfurt Institute for Advanced Studies, Johann Wolfgang Goethe-Universität Frankfurt, Frankfurt, Germany*
[22]*Department of Physics and Technology, University of Bergen, Bergen, Norway*
[23]*V. Fock Institute for Physics, St. Petersburg State University, St. Petersburg, Russia*
[24]*Universidade de São Paulo (USP), São Paulo, Brazil*
[25]*National Institute for Physics and Nuclear Engineering, Bucharest, Romania*
[26]*Research Division and ExtreMe Matter Institute EMMI, GSI Helmholtzzentrum für Schwerionenforschung, Darmstadt, Germany*
[27]*Physikalisches Institut, Ruprecht-Karls-Universität Heidelberg, Heidelberg, Germany*
[28]*Institut für Kernphysik, Westfälische Wilhelms-Universität Münster, Münster, Germany*
[29]*Rudjer Bošković Institute, Zagreb, Croatia*
[30]*Sezione INFN, Padova, Italy*
[31]*SUBATECH, Ecole des Mines de Nantes, Université de Nantes, CNRS-IN2P3, Nantes, France*
[32]*Institut für Kernphysik, Johann Wolfgang Goethe-Universität Frankfurt, Frankfurt, Germany*
[33]*Departamento de Física de Partículas and IGFAE, Universidad de Santiago de Compostela, Santiago de Compostela, Spain*
[34]*European Organization for Nuclear Research (CERN), Geneva, Switzerland*
[35]*Oak Ridge National Laboratory, Oak Ridge, Tennessee, USA*
[36]*Physics Department, University of Cape Town, Cape Town, South Africa*
[37]*Sezione INFN, Catania, Italy*
[38]*Laboratoire de Physique Corpusculaire (LPC), Clermont Université, Université Blaise Pascal, CNRS-IN2P3, Clermont-Ferrand, France*
[39]*Gangneung-Wonju National University, Gangneung, South Korea*
[40]*Physics Department, University of Jammu, Jammu, India*
[41]*Commissariat à l'Energie Atomique, IRFU, Saclay, France*
[42]*Institute of Physics, Bhubaneswar, India*
[43]*Dipartimento di Fisica e Astronomia dell'Università and Sezione INFN, Catania, Italy*
[44]*Dipartimento Interateneo di Fisica 'M. Merlin' and Sezione INFN, Bari, Italy*
[45]*Wigner Research Centre for Physics, Hungarian Academy of Sciences, Budapest, Hungary*
[46]*The Henryk Niewodniczanski Institute of Nuclear Physics, Polish Academy of Sciences, Cracow, Poland*
[47]*Joint Institute for Nuclear Research (JINR), Dubna, Russia*
[48]*Department of Physics, University of Oslo, Oslo, Norway*
[49]*Niels Bohr Institute, University of Copenhagen, Copenhagen, Denmark*
[50]*Institut Pluridisciplinaire Hubert Curien (IPHC), Université de Strasbourg, CNRS-IN2P3, Strasbourg, France*
[51]*University of Houston, Houston, Texas, USA*
[52]*Instituto de Física, Universidad Nacional Autónoma de México, Mexico City, Mexico*
[53]*Wayne State University, Detroit, Michigan, USA*
[54]*Moscow Engineering Physics Institute, Moscow, Russia*
[55]*Dipartimento di Fisica dell'Università and Sezione INFN, Turin, Italy*
[56]*St. Petersburg State Polytechnical University*
[57]*Petersburg Nuclear Physics Institute, Gatchina, Russia*
[58]*Physik Department, Technische Universität München, Munich, Germany*
[59]*Institute for Subatomic Physics of Utrecht University, Utrecht, Netherlands*
[60]*Gauhati University, Department of Physics, Guwahati, India*
[61]*University of Tsukuba, Tsukuba, Japan*
[62]*Laboratori Nazionali di Frascati, INFN, Frascati, Italy*
[63]*Centro de Investigaciones Energéticas Medioambientales y Tecnológicas (CIEMAT), Madrid, Spain*
[64]*Lawrence Berkeley National Laboratory, Berkeley, California, USA*
[65]*SSC IHEP of NRC Kurchatov institute, Protvino, Russia*
[66]*Faculty of Science, P. J. Šafárik University, Košice, Slovakia*
[67]*Pusan National University, Pusan, South Korea*
[68]*iThemba LABS, National Research Foundation, Somerset West, South Africa*

[69]*Nikhef, National Institute for Subatomic Physics, Amsterdam, Netherlands*
[70]*Institut für Informatik, Johann Wolfgang Goethe-Universität Frankfurt, Frankfurt, Germany*
[71]*Purdue University, West Lafayette, Indiana, USA*
[72]*Russian Federal Nuclear Center (VNIIEF), Sarov, Russia*
[73]*Dipartimento di Fisica e Astronomia dell'Università and Sezione INFN, Padova, Italy*
[74]*Central China Normal University, Wuhan, China*
[75]*Sección Física, Departamento de Ciencias, Pontificia Universidad Católica del Perú, Lima, Peru*
[76]*Dipartimento di Fisica dell'Università and Sezione INFN, Trieste, Italy*
[77]*Dipartimento di Fisica dell'Università and Sezione INFN, Cagliari, Italy*
[78]*Centro de Aplicaciones Tecnológicas y Desarrollo Nuclear (CEADEN), Havana, Cuba*
[79]*University of Jyväskylä, Jyväskylä, Finland*
[80]*Saha Institute of Nuclear Physics, Kolkata, India*
[81]*Physics Department, Creighton University, Omaha, Nebraska, USA*
[82]*Université de Lyon, Université Lyon 1, CNRS/IN2P3, IPN-Lyon, Villeurbanne, France*
[83]*Division of Experimental High Energy Physics, University of Lund, Lund, Sweden*
[84]*Sezione INFN, Cagliari, Italy*
[85]*Laboratoire de Physique Subatomique et de Cosmologie, Université Grenoble-Alpes, CNRS-IN2P3, Grenoble, France*
[86]*Institut de Physique Nucléaire d'Orsay (IPNO), Université Paris-Sud, CNRS-IN2P3, Orsay, France*
[87]*Centro de Investigación y de Estudios Avanzados (CINVESTAV), Mexico City and Mérida, Mexico*
[88]*Dipartimento di Scienze e Innovazione Tecnologica dell'Università del Piemonte Orientale and Gruppo Collegato INFN, Alessandria, Italy*
[89]*Benemérita Universidad Autónoma de Puebla, Puebla, Mexico*
[90]*Instituto de Ciencias Nucleares, Universidad Nacional Autónoma de México, Mexico City, Mexico*
[91]*Institute of Space Science (ISS), Bucharest, Romania*
[92]*Bose Institute, Department of Physics and Centre for Astroparticle Physics and Space Science (CAPSS), Kolkata, India*
[93]*Universidade Estadual de Campinas (UNICAMP), Campinas, Brazil*
[94]*National Centre for Nuclear Studies, Warsaw, Poland*
[95]*Dipartimento di Fisica "E.R. Caianiello" dell'Università and Gruppo Collegato INFN, Salerno, Italy*
[96]*Sezione INFN, Bari, Italy*
[97]*Sezione INFN, Rome, Italy*
[98]*Helsinki Institute of Physics (HIP), Helsinki, Finland*
[99]*University of Liverpool, Liverpool, United Kingdom*
[100]*Institute for Nuclear Research, Academy of Sciences, Moscow, Russia*
[101]*Physics Department, University of Athens, Athens, Greece*
[102]*Sezione INFN, Trieste, Italy*
[103]*Department of Physics, Ohio State University, Columbus, Ohio, USA*
[104]*Chicago State University, Chicago, Illinois, USA*
[105]*Technical University of Split FESB, Split, Croatia*
[106]*Warsaw University of Technology, Warsaw, Poland*
[107]*A.I. Alikhanyan National Science Laboratory (Yerevan Physics Institute) Foundation, Yerevan, Armenia*
[108]*University of Tokyo, Tokyo, Japan*
[109]*Eberhard Karls Universität Tübingen, Tübingen, Germany*
[110]*Institute of Physics, Academy of Sciences of the Czech Republic, Prague, Czech Republic*
[111]*Department of Physics, Sejong University, Seoul, South Korea*
[112]*Institute of Experimental Physics, Slovak Academy of Sciences, Košice, Slovakia*
[113]*Yonsei University, Seoul, South Korea*
[114]*KTO Karatay University, Konya, Turkey*
[115]*Zentrum für Technologietransfer und Telekommunikation (ZTT), Fachhochschule Worms, Worms, Germany*
[116]*Department of Applied Physics, Aligarh Muslim University, Aligarh, India*
[117]*California Polytechnic State University, San Luis Obispo, California, USA*
[118]*The University of Texas at Austin, Physics Department, Austin, Texas, USA*
[119]*Suranaree University of Technology, Nakhon Ratchasima, Thailand*
[120]*Vestfold University College, Tonsberg, Norway*
[121]*Nuclear Physics Group, STFC Daresbury Laboratory, Daresbury, United Kingdom*
[122]*Universidad Autónoma de Sinaloa, Culiacán, Mexico*
[123]*M.V. Lomonosov Moscow State University, D.V. Skobeltsyn Institute of Nuclear Physics, Moscow, Russia*
[124]*University of Tennessee, Knoxville, Tennessee, USA*
[125]*Dipartimento di Fisica dell'Università "La Sapienza" and Sezione INFN, Rome, Italy*
[126]*Faculty of Mathematics, Physics and Informatics, Comenius University, Bratislava, Slovakia*
[127]*University of Belgrade, Faculty of Physics and "Vinča" Institute of Nuclear Sciences, Belgrade, Serbia*

[128] *Indian Institute of Technology Indore, Indore (IITI), India*
[129] *National Institute of Science Education and Research, Bhubaneswar, India*
[130] *Budker Institute for Nuclear Physics, Novosibirsk, Russia*
[131] *University of Zagreb, Zagreb, Croatia*
[132] *Physics Department, University of Rajasthan, Jaipur, India*
[133] *Institute of Theoretical Physics, University of Wroclaw, Wroclaw, Poland*
[134] *Laboratori Nazionali di Legnaro, INFN, Legnaro, Italy*
[135] *Hiroshima University, Hiroshima, Japan*
[136] *University of Kansas, Lawrence, Kansas, USA*
[137] *Centre de Calcul de l'IN2P3, Villeurbanne, France*

[*] Deceased
[†] Permanent address: Konkuk University, Seoul, Korea.